

Porous microneedle patch with sustained delivery of extracellular vesicles mitigates severe spinal cord injury

Received: 25 July 2022

Accepted: 23 June 2023

Published online: 07 July 2023

 Check for updates

Ao Fang^{1,2,3,4,8}, Yifan Wang^{1,4,8}, Naiyu Guan^{1,2,3,4,8}, Yanming Zuo^{1,2,3,8}, Lingmin Lin^{2,3}, Binjie Guo^{2,3}, Aisheng Mo^{2,3}, Yile Wu^{2,3}, Xurong Lin^{2,3}, Wanxiong Cai^{2,3}, Xiangfeng Chen^{2,3,4}, Jingjia Ye^{2,3,4}, Zeinab Abdelrahman^{1,2,3,4}, Xiaodan Li^{1,2,3,4}, Hanyu Zheng^{2,3}, Zhonghan Wu^{2,3}, Shuang Jin^{2,3}, Kan Xu⁴, Yan Huang⁵, Xiaosong Gu⁶, Bin Yu⁶ & Xuhua Wang^{1,2,3,4,7} ✉

The transplantation of mesenchymal stem cells-derived secretome, particularly extracellular vesicles is a promising therapy to suppress spinal cord injury-triggered neuroinflammation. However, efficient delivery of extracellular vesicles to the injured spinal cord, with minimal damage, remains a challenge. Here we present a device for the delivery of extracellular vesicles to treat spinal cord injury. We show that the device incorporating mesenchymal stem cells and porous microneedles enables the delivery of extracellular vesicles. We demonstrate that topical application to the spinal cord lesion beneath the spinal dura, does not damage the lesion. We evaluate the efficacy of our device in a contusive spinal cord injury model and find that it reduces the cavity and scar tissue formation, promotes angiogenesis, and improves survival of nearby tissues and axons. Importantly, the sustained delivery of extracellular vesicles for at least 7 days results in significant functional recovery. Thus, our device provides an efficient and sustained extracellular vesicles delivery platform for spinal cord injury treatment.

There are approximately 930,000 new spinal cord injury (SCI) cases caused by accidents each year¹. Even though the systemic administration of methylprednisolone sodium succinate (MPSS) has been approved as the only drug for treating acute SCI, this drug has limited therapeutic efficacy and severe side effects, which severely limits its application in clinical practice^{2,3}. SCI is initially caused by mechanical trauma and diverse mechanisms of secondary damage following the

inflammatory response⁴. Secondary damage can cause hemorrhage, edema, decreased blood flow and inflammation, thus affecting adjacent spinal cord segments⁵. The inflammatory environment triggered by the activation of microglia and the release of proinflammatory cytokines leads to inevitable neuronal damage and, consequently, scar and cystic cavity formation in spinal cord lesion sites^{6,7}. Recently, extensive studies have demonstrated that mesenchymal stem cells

¹Department of Rehabilitation Medicine of First Affiliated Hospital and School of Brain Science and Brain Medicine, Zhejiang University School of Medicine, 310003 Hangzhou, Zhejiang Province, P. R. China. ²Liangzhu Laboratory, MOE Frontier Science Center for Brain Science and Brain-machine Integration, State Key Laboratory of Brain-machine Intelligence, Zhejiang University, 1369 West Wenyi Road, 311121 Hangzhou, China. ³NHC and CAMS Key Laboratory of Medical Neurobiology, Zhejiang University, 310058 Hangzhou, China. ⁴Department of Orthopedics of 2nd Affiliated Hospital and School of Brain Science and Brain Medicine, Zhejiang University School of Medicine, Zhejiang University, 310003 Hangzhou Zhejiang Province PR China. ⁵Department of Hepatobiliary and Pancreatic Surgery, Affiliated Hospital of Nantong University, Medical School of Nantong University, 226001 Nantong, China. ⁶Key Laboratory of Neuroregeneration of Jiangsu and Ministry of Education, NMPA Key Laboratory for Research and Evaluation of Tissue Engineering Technology Products, Nantong University, Nantong, China. ⁷Co-innovation Center of Neuroregeneration, Nantong University, 226001 Nantong, Jiangsu, P. R. China. ⁸These authors contributed equally: Ao Fang, Yifan Wang, Naiyu Guan, Yanming Zuo. ✉e-mail: xhw@zju.edu.cn

(MSCs) delivered intravenously (IV) promote functional recovery after contusive SCI^{8–11}. However, the lung has the ability to clear over 60% of the administered MSCs, resulting in a decrease in the number of MSCs that can be home to the lesion site to the injured site and play a therapeutic role¹². Although some cells in the lungs might survive for 2–3 days and release exosomes which can potentially travel to the target injury site, the patients may experience coughing side effects^{13,14}. Alternatively, the transplantation of MSCs directly into the lesion site has been proposed as an effective treatment to alleviate neuroinflammation triggered by SCI¹⁵. However, the neuroinflammatory microenvironments of spinal cord injury (SCI) lesions have been shown to be detrimental to the survival and function of mesenchymal stem cells (MSCs), thus posing a significant obstacle to the clinical application of these cells¹¹.

Fortunately, it has been reported that MSC secretome, particularly extracellular vesicles (MSC-EVs), offer similar therapeutic benefits for immune modulation in animal models of SCI^{16–18}. Previous studies have shown that MSC-EVs immobilized in a peptide-modified adhesive hydrogel transplanted into an SCI lesion during the acute phase could mitigate the SCI microenvironment and promote functional recovery^{19–21}. However, the retention time of MSC-EVs in spinal tissue by directly transplantation might not be long enough for them to exhibit their optimal therapeutic effects^{17,22}. The neuroinflammation and neuronal apoptosis caused by SCI could continue for a couple of weeks or even longer⁴, but MSC-EVs could not be continuously delivered to SCI lesions by these methods. Moreover, direct transplantation

of MSCs or MSC-EVs into the spinal cord injury site may result in damage to healthy tissues adjacent to the lesion, potentially leading to unpredictable side effects²³. Therefore, direct transplantation of materials containing MSCs or MSC-EVs into the spinal cord lesion of an acute SCI patient is not an optimized approach.

To overcome these challenges, we took advantage of a microneedle (MN) array, which has facilitated painless localized delivery of drugs or therapeutic biomolecules with good tolerability in clinical trials^{24–26}. We then fabricated a patch with an MN array with appropriate mechanical strength matching soft spinal tissues and with a suitable pore size for MSC-EV delivery when it was mounted onto a spinal cord lesion beneath the dura^{27,28}. To sustainably deliver MSC-EVs, the MN arrays were additionally mounted with a gelatin methacryloyl (GelMA) hydrogel block embedded with MSCs during surgery (Fig. 1). We envisioned that the GelMA hydrogel block could provide a biocompatible microenvironment for promoting the long-term survival of MSCs. In this way, we achieved a sustained delivery of MSC secretome to the spinal cord lesion via the use of porous MNs. This approach was proposed to enhance therapeutic efficacy without requiring direct invasion of MSCs into the spinal cord (Fig. 1). We showed that MN-MSC patch can effectively maintain the survival of MSCs and sustainably release MSC secretome for at least one week, which led to remarkable neuroprotection effects, superior muscle control, and robust functional recovery following severe SCI (Fig. 1).

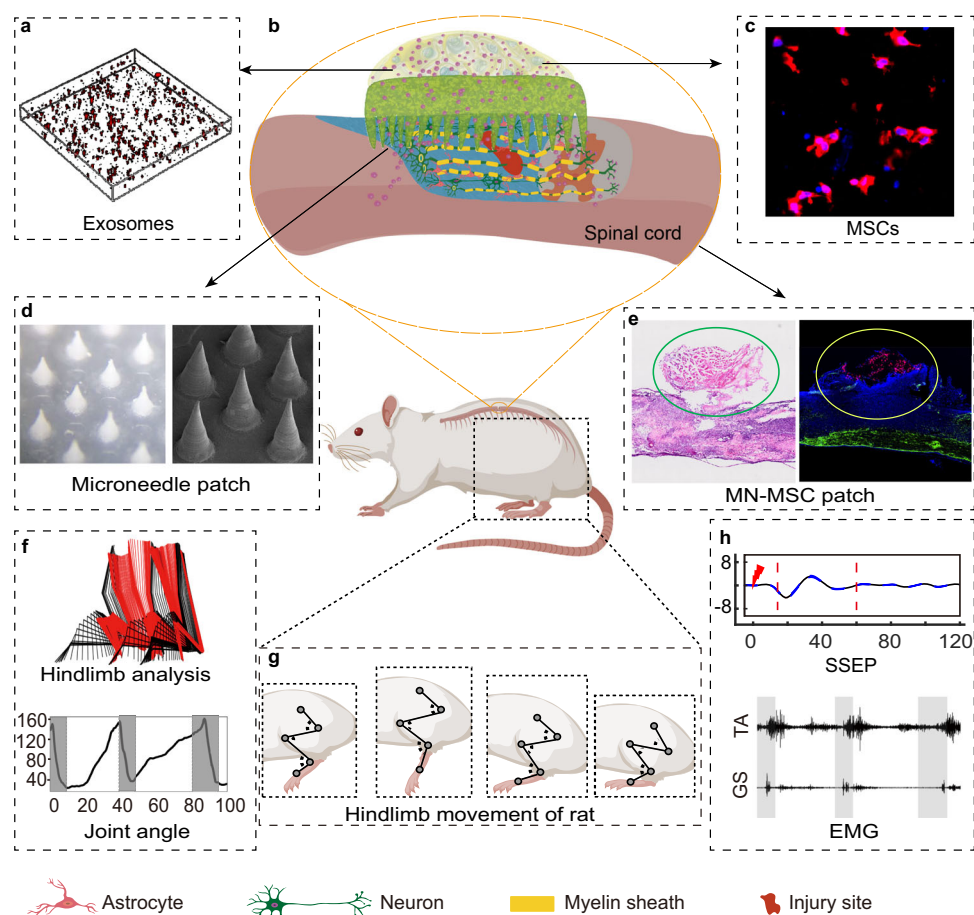


Fig. 1 | Schematic illustration of MN-MSC patch implantation at the site of the spinal cord injury. **a** Schematic depicting exosomes embedded in GelMA hydrogel. **b** Schematic of the MN-MSC patch. **c** Representative microscopy images showing MSCs in the patch. **d** Representative morphological images of the

Microneedle patch. **e** Representative microscopy images of the MN-MSC patch applied to the spinal cord. **f** Analysis of hindlimb function including joint angle. **g** Illustration of hindlimb movement. **h** Electrophysiological analysis of hindlimb movement.

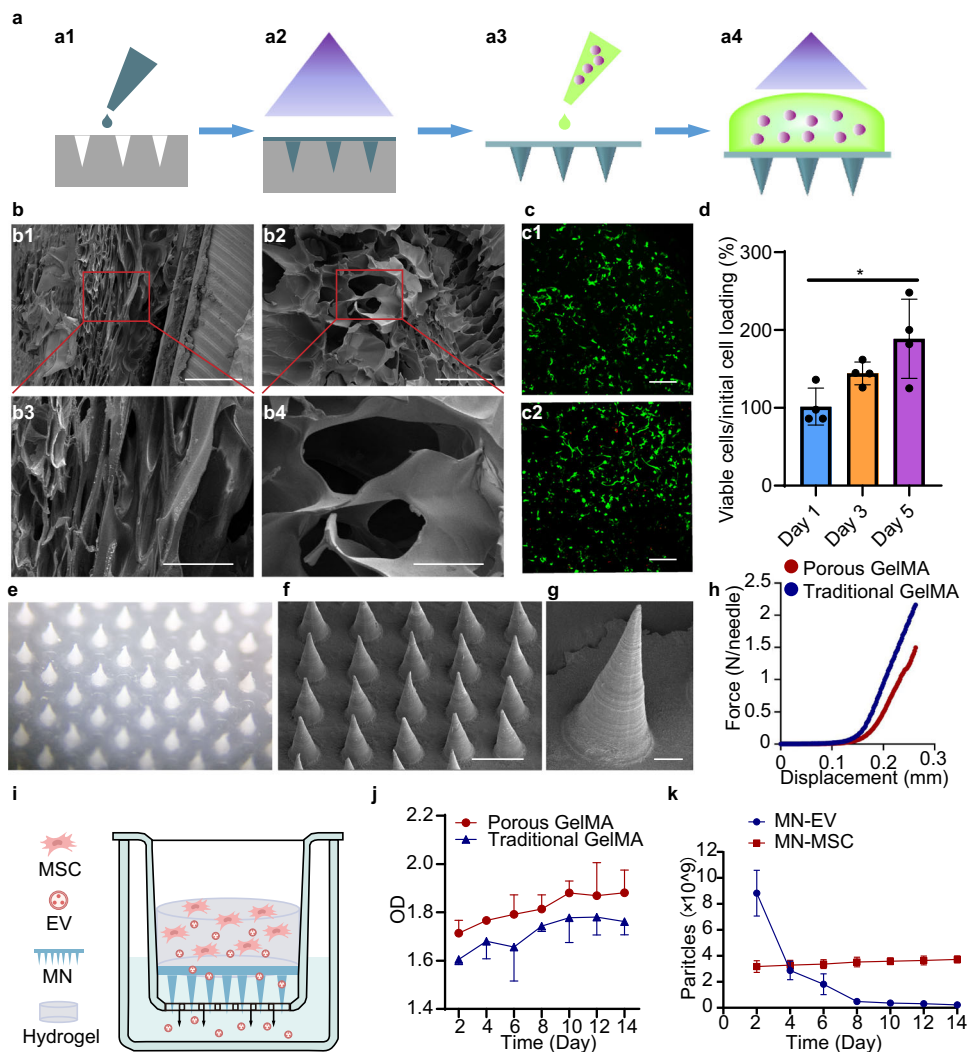


Fig. 2 | Fabrication and characterization of the MN-MSc patch. **a** Schematic of the MN-MSc patch fabrication process by a1) casting, a2) blue light crosslinking, a3) peeling from the PDMS mold and adding GelMA solution with MSCs, and a4) blue light crosslinking. **b** SEM image of the b1) interstructure of traditional and b2) porous GelMA hydrogels. Scale bars of images (b1, b2) indicate 300 μm , and scale bars of images (b3, b4) indicate 100 μm . The experiment was repeated 3 times independently with similar results. **c** Calcein AM (live)/EthD (dead) staining revealed the morphology and viability of MSCs encapsulated in GelMA hydrogel on c1) day 3 and c2) day 5. Scale bars: 200 μm . **d** Quantitative viability analysis of MSCs encapsulated in GelMA hydrogel on days 1, 3 and 5. Data are presented as the means \pm SEM ($n = 4$ independent GelMA hydrogels with MSCs). Statistical analysis was performed using one-way ANOVA followed by Tukey's multiple comparisons

test and two-tailed paired t tests were used for comparisons between two groups. Total: $F = 6.808$, $p = 0.0158$. Day 1 vs Day 3, $p = 0.2211$; Day 1 vs Day 5, $p = 0.0125$; Day 3 vs Day 5, $p = 0.1994$. * indicates $p < 0.05$. **e** Representative optical microscopy images and (f, g) SEM images of MNs. Scale bars for images (f) indicate 500 μm , and scale bars for images (g) indicate 50 μm . The experiment was repeated 3 times independently with similar results. **h** The mechanical strength of MNs. **i** Schematic showing the study design used to test the release profile of exosomes from the MN-MSc patch. **j** The daily proteins release curves of MN-MSc patches fabricated with porous and normal GelMA hydrogels. Data are presented as the means \pm SEM ($n = 3$ independent patches for each group). **k** The daily exosome release curves of MN-MSc and MN-EV patches. Data are presented as the means \pm SEM ($n = 3$ independent patches for each group).

Results

Fabrication and characterization of the patch with an MN array In Vitro

To characterize the produced MSCs, we conducted flow cytometry analysis. According to well-accepted criteria for the identification of specific cell-surface markers (that is, CD73⁺, CD90⁺, CD105⁺, CD45⁻, CD34⁻, CD19⁻, CD14⁻, CD11b⁻, CD79a⁻, and HLA-DR⁹), the harvested cells were identified as MSCs (Fig. S1), suggesting the high quality of MSCs used in our study. To achieve sustainable release of MSC secretome, we designed a patch containing an MN array (Fig. 2a). The MN patch was made from chemically cross-linked methacryloyl (MW, 250 kDa) with a micromolding method to form GelMA (Fig. 2a, a1, a2)^{29,30}. The scale of the fabricated MN patch was approximately 4 mm \times 4 mm with 45 needles, which is large enough to cover a typical rat contusive spinal

cord lesion (Fig. S3). The needle of the MN arrays was conical, with a base diameter of 250 μm , a height of 600 μm and a tip diameter of 10 μm (Fig. 2e–g). To sustainably release extracellular vesicles, the patch was additionally covered with GelMA hydrogel embedded with MSCs during surgery (Fig. S3f–i). The GelMA hydrogel with porous structures was designed to facilitate the release of MSC-EVs through the polymeric needles. As shown in the scanning electron microscopy (SEM) images, the pore size of the gel reached up to approximately 100 μm (Fig. 2b, b2, b4), compared with the relatively small pore size of 10 μm in the traditional GelMA hydrogel (Fig. 2b, b1, b3).

To examine the biocompatibility of the MN patch, we first dropped the methacryloyl solution with MSCs (40 μl , approximately 2.5×10^7 cells/mL) onto the surface of the patch and cross-linked methacryloyl to form GelMA hydrogel with blue light irradiation (Fig. 2a, a3,

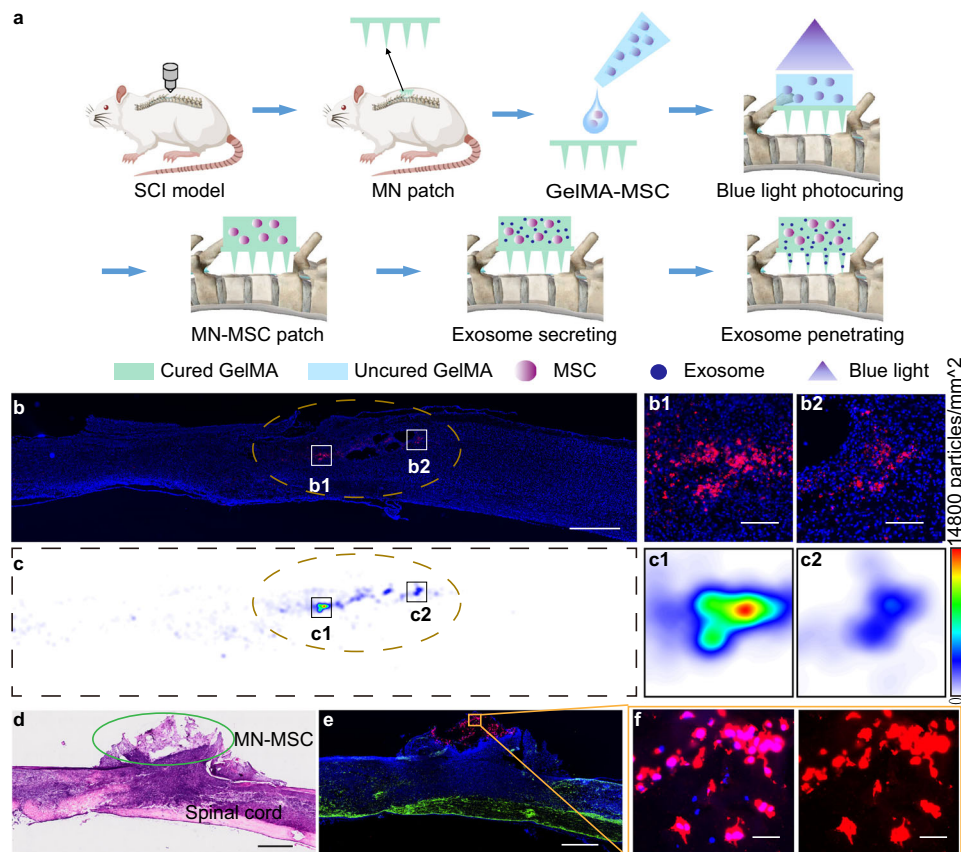


Fig. 3 | Sustained MSC-EV delivery by MN-MSC patch treatment alleviates neuroinflammation triggered by SCI. **a** Schematic illustration of MN-MSC patch implantation on the injury site of the spinal cord. **b** In vivo distribution of exosomes (Dil labeled, red) in the injured spinal cord tissues after MN-EV patch implantation, blue (DAPI). Scale bar: 1 mm. The injury region of the spinal cord is marked with yellow dotted lines. **c** Heatmaps of exosome distribution in the injured spinal cord tissues after MN-EV patch implantation; red: the highest numbers of exosomes, blue: the lowest, and white: background. The injury region of the spinal cord is marked with yellow dotted lines. b1, b2, c1, c2) Enlarged images to show the details.

Scale bar: 100 μ m. **d** HE staining of the injured spinal cord with MN-MSC patch implantation; scale bar: 1 mm. The experiment was repeated 3 times independently with similar results. **e** Representative images of immunohistochemical staining for MN-MSC patches on the injured spinal cord on day 7 after SCI. Green (GFAP), blue (DAPI), red (GAPDH), scale bar: 1 mm. The experiment was repeated 3 times independently with similar results. **f** High-magnification images of the boxed area, scale bar: 50 μ m. The experiment was repeated 3 times independently with similar results.

a4). The live/dead staining of the GelMA hydrogel revealed excellent viability of embedded MSCs after culturing for 3 and 5 days (Fig. 2c). Quantitative analysis with the CCK-8 test indicated that MSCs in the GelMA hydrogel of the MN-MSC patch survived and proliferated well (Fig. 2d). The needle with a porous structure exhibited comparatively lower mechanical strength than the conventional needle (porous 10.77 kPa vs traditional 30.92 kPa, Fig. S3e), and matched that of the soft rat's spinal cord tissues (around 8.1 kPa)^{27,28}. We next assessed the MSC-EV release capacity of the MN patch with this porous structure. To do so, the patches made from porous GelMA²⁶ or regular GelMA were seeded with MSCs and placed in the upper compartment of a Transwell (Fig. 2i). The Transwells were then immersed in culture media and incubated at 37 °C. At regular intervals, aliquots of samples were collected from the bottom wells, and the concentrations of MSC-secretomes in the samples were measured by a Micro BCA Protein Assay kit³¹. Plotting the optical density (OD) of the samples revealed that the MN patch made from porous GelMA released MSC-secretome more efficiently (Fig. 2j), possibly because the MN patch with a larger pore size was more permeable for MSC-secretome. We therefore chose the MN patch made from porous GelMA for the following studies.

Previous studies have demonstrated that extracellular vesicles (EVs) derived from stem cells show promise as a potential alternative to stem cell therapy^{16–18}, we therefore sought to evaluate the sustained MSC-EVs delivery capacity of MN patches embedded with MSCs (MN-

MSC). The MN patches directly loaded with MSC-EVs (MN-EV) were used as controls. The MSC-EVs were isolated from MSC culture supernatant via ultracentrifugation and showed a typical cup-shaped morphology (Fig. S2a). Through nanoparticle tracking analysis (NTA), we found that the MSC-EVs had an average size of 110 nm, which was consistent with the results of previous studies (Fig. S2c)^{20,32}. The expression of tetrapanins CD9 and TSG101 (mesenchymal markers) on the collected samples (Fig. S2d) indicated successful isolation and purification of MSC-EVs. We then compared the persistent MSC-EV release capacity of MSC-seeded and MSC-EV-loaded MN patches. The numbers of MSC-EVs released in the collected samples from the lower wells of the Transwell system at various time points were plotted (Fig. 2k). The results indicated that the release of MSC-EVs from MSC-EV-loaded MN patches initially declined rapidly within the first 4 days, whereas the delivery of MSC-EVs from MSC-seeded MN patches remained stable, with a slight increase at 2 weeks (Fig. 2k). This suggests that the MN patches exhibited excellent biocompatibility, allowing for the survival of MSCs. Thus, we successfully fabricated a device for the sustained and efficient delivery of MSC-EVs.

Distribution of EVs in the injured spinal cord after MN patch implantation

After verifying that the fabricated MN-MSC patch could sustainably deliver EVs in vitro, we sought to assess whether the MSC-EVs of the

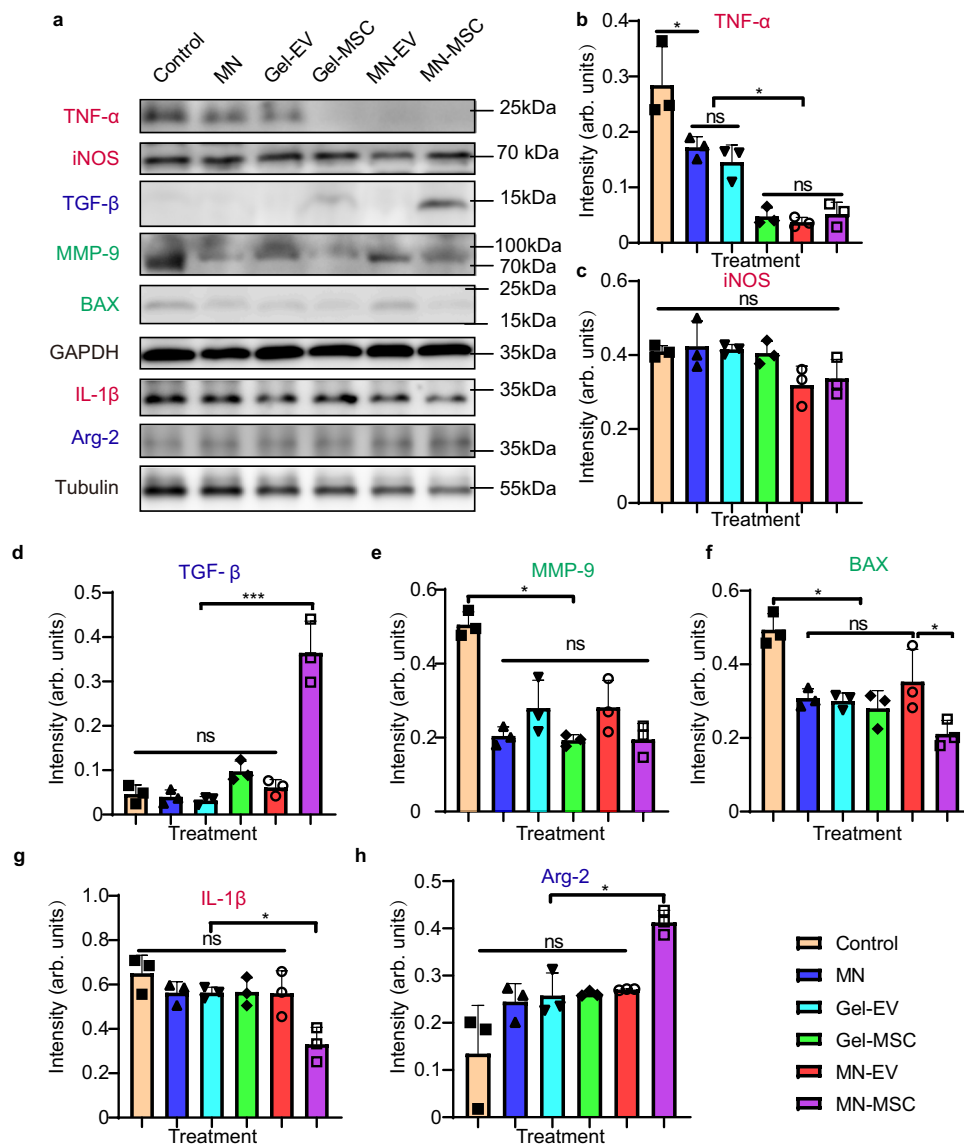


Fig. 4 | Genetic expression analysis of the injured spinal cord tissues.

a Representative immunoblots showing expression of TNF- α , iNOS, MMP-9, TGF- β , BAX, IL-1 β , and Arg-2 in the injury site 1 week after SCI (red font represents proinflammatory markers, blue font represents anti-inflammatory markers, and green font represents anti-apoptotic/inflammatory markers; GAPDH and Tubulin were used as loading controls). The experiment was repeated 3 times independently with similar results. **b–h** Quantitative analyses of the genetic expression levels of TNF- α (**b**), iNOS (**c**), TGF- β (**d**), MMP-9 (**e**), BAX (**f**), IL-1 β (**g**), and Arg-2 (**h**) in the injury site. $n = 3$ animals chosen randomly from each group. Data are presented as the mean \pm SEM. Statistical analysis was performed using one-way

ANOVA followed by Tukey's multiple comparisons test and two-tailed paired t tests were used for comparisons between two groups. ANOVA for TNF- α : Total: $F = 24.27$, $p < 0.0001$, Control vs MN, $p = 0.0164$, Gel-EV vs MN-MSC, $p = 0.0493$. ANOVA for iNOS: Total: $F = 3.178$, $p = 0.0468$. ANOVA for TGF- β : Total: $F = 43.96$, $p < 0.0001$. MN-EV vs. MN-MSC, $p < 0.0001$. ANOVA for MMP-9: Total: $F = 17.14$, $p < 0.0001$. Control vs MN-MSC, $p < 0.0001$. ANOVA for BAX: Total: $F = 11.18$, $p = 0.0003$. Control vs MN-EV, $p = 0.0391$. MN-EV vs MN-MSC, $p = 0.0373$. ANOVA for IL-1 β : Total: $F = 6.960$, $p = 0.0029$. MN-EV vs MN-MSC, $p = 0.0178$. ANOVA for Arg-2: Total: $F = 9.560$, $p = 0.0007$. MN-EV vs MN-MSC, $p = 0.0388$. * $p < 0.05$, ** $p < 0.01$, *** $p < 0.001$.

patch could be delivered through the MNs into injured spinal cord tissues in a contusive rat SCI model. We used a severe T10 contusive SCI model, which was constructed by an infinite vertical impactor with the parameters of a 2.5 m/s rate, 2 mm depth, 5 s duration time and 3 mm diameter cylinder³³. Because MSC-EVs in live MSCs are difficult to label, MSC-EVs stained with CM-Dil were encapsulated in GelMA hydrogels in this experiment. The red fluorescence of MSC-EVs encapsulated in the GelMA hydrogel indicated their successful labeled with CM-Dil (Fig. S2b). After contusive SCI, the dura of the spinal cord was removed carefully by a pair of surgical scissors. Then, the MN patch was placed on top of the spinal cord lesion, and a solution of GelMA mixed with MSC-EVs was mounted on the top of

the MN patch, followed by a blue light photocuring process (Fig. 3a). Seven days after surgery, we found that most of the released MSC-EVs were localized and aggregated in the spinal injury site (Fig. 3b, c, b1, b2, c1, c2), indicating the localized delivery capacity of the MN patch. Therefore, we concluded that the MN patch has excellent localized delivery capacity of MSC-EVs in vivo, which facilitates sustained MSC-EV delivery for SCI treatment.

Next, we attempted to assess whether the cells in the MN-MSC patch survived long enough to ameliorate the SCI-induced neuroinflammatory environment and protect the spared tissues/axons from secondary injuries. We implanted the MN patch into the spinal cord lesion of the same SCI model, and the solution of MSCs mixed with

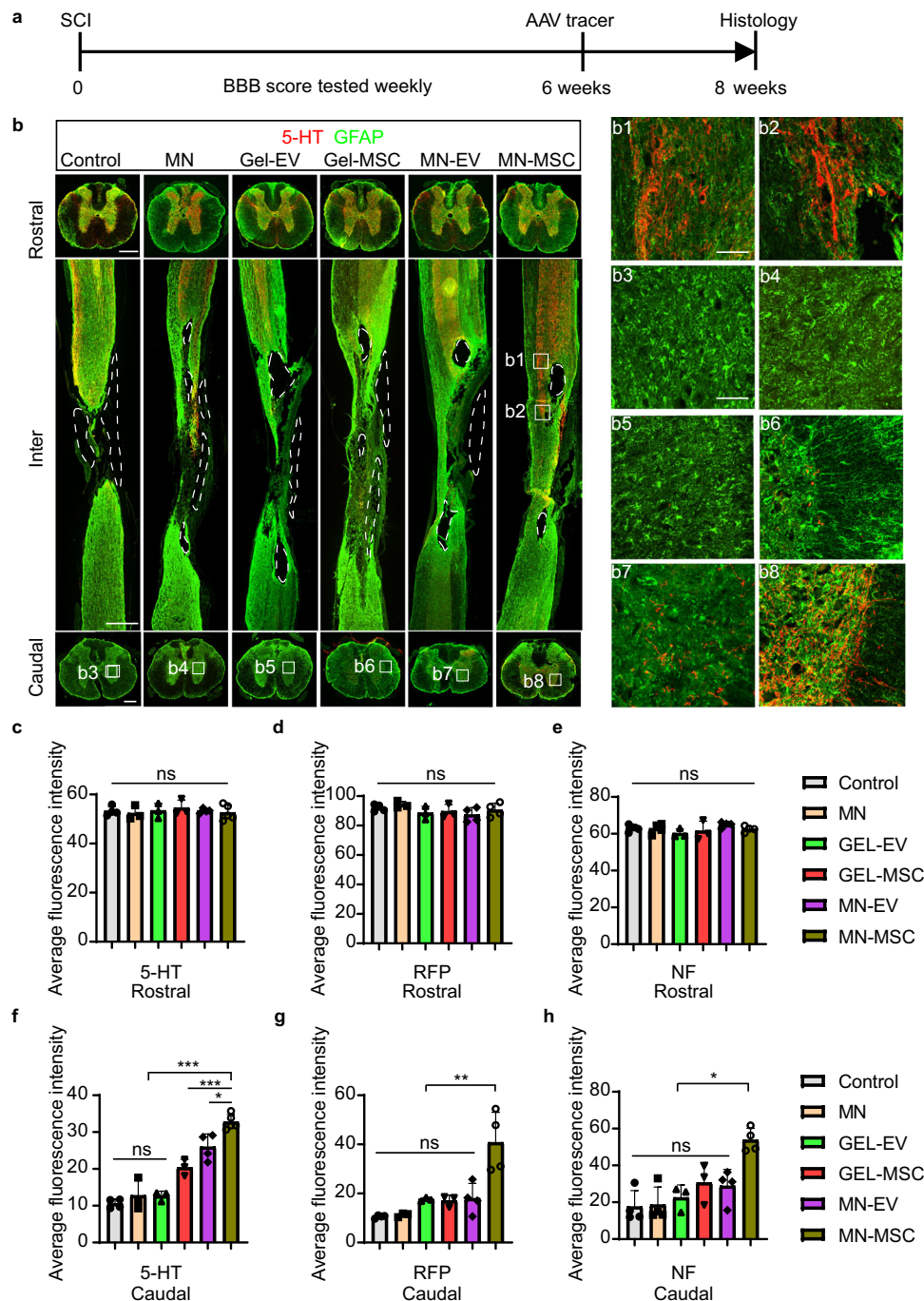


Fig. 5 | Protection of spared axons with MN-MSC patch treatment after SCI.

a Schematic diagram of the experimental design. The MN or MN-MSC patch was implanted 3 h after SCI, the AAV tracer for axons was injected at 6 weeks after injury, and the histological study was performed at 8 weeks after injury.

b Representative images of spinal sections stained with GFAP (green) and 5-HT (red) of rats in the six groups at 8 weeks after SCI. Solid lines indicate the boundary of the cavities. Scale bars for rostral and caudal indicate 500 μ m and inter indicate 1 mm. b1–b8 show the details of the black boundary area, and the scale bars are 100 μ m. Representative images of propriospinal axons (RFP labeled, Fig. S6) and NF axons (Fig. S7) in SCI rats with different treatments are shown in supplementary figures. **c–h** Quantification of the average fluorescence intensity of 5-HT (**c**), RFP (**d**), and NF (**e**) immunoreactivity on the rostral and caudal sides of the six groups with 5-HT (**f**), RFP (**g**), and NF (**h**) staining. Data are shown as the mean \pm SEM.

Statistical analysis was performed using one-way ANOVA followed by Tukey's multiple comparisons test and two-tailed paired *t* tests were used for comparisons between two groups. Control: $n_{5-HT} = 4$, $n_{RFP} = 4$, $n_{NF} = 4$. MN: $n_{5-HT} = 3$, $n_{RFP} = 3$, $n_{NF} = 4$. Gel-EV: $n_{5-HT} = 3$, $n_{RFP} = 3$, $n_{NF} = 3$. Gel-MN: $n_{5-HT} = 3$, $n_{RFP} = 3$, $n_{NF} = 3$. MN-EV: $n_{5-HT} = 4$, $n_{RFP} = 4$, $n_{NF} = 4$. MN-MSC: $n_{5-HT} = 5$, $n_{RFP} = 4$, $n_{NF} = 4$. These animals chosen randomly from each group. ANOVA for 5-HT of rostral: Total: $F = 0.2836$, $p = 0.9152$. ANOVA for 5-HT of caudal: Total: $F = 47.76$, $p < 0.0001$, Control vs MN-MSC, $p < 0.0001$, GEL-MSC vs MN-MSC, $p < 0.0001$, MN-EV vs MN-MSC, $p = 0.0134$. ANOVA for RFP of rostral: Total: $F = 1.243$, $p = 0.3380$. ANOVA for RFP of caudal: Total: $F = 12.13$, $p < 0.0001$, MN-EV vs MN-MSC, $p = 0.0013$. ANOVA for NF of rostral: Total: $F = 1.167$, $p = 0.3675$. ANOVA for NF of caudal: Total: $F = 9.322$, $p = 0.0003$, MN-EV vs MN-MSC, $p = 0.01$. * $p < 0.05$, ** $p < 0.01$, *** $p < 0.001$.

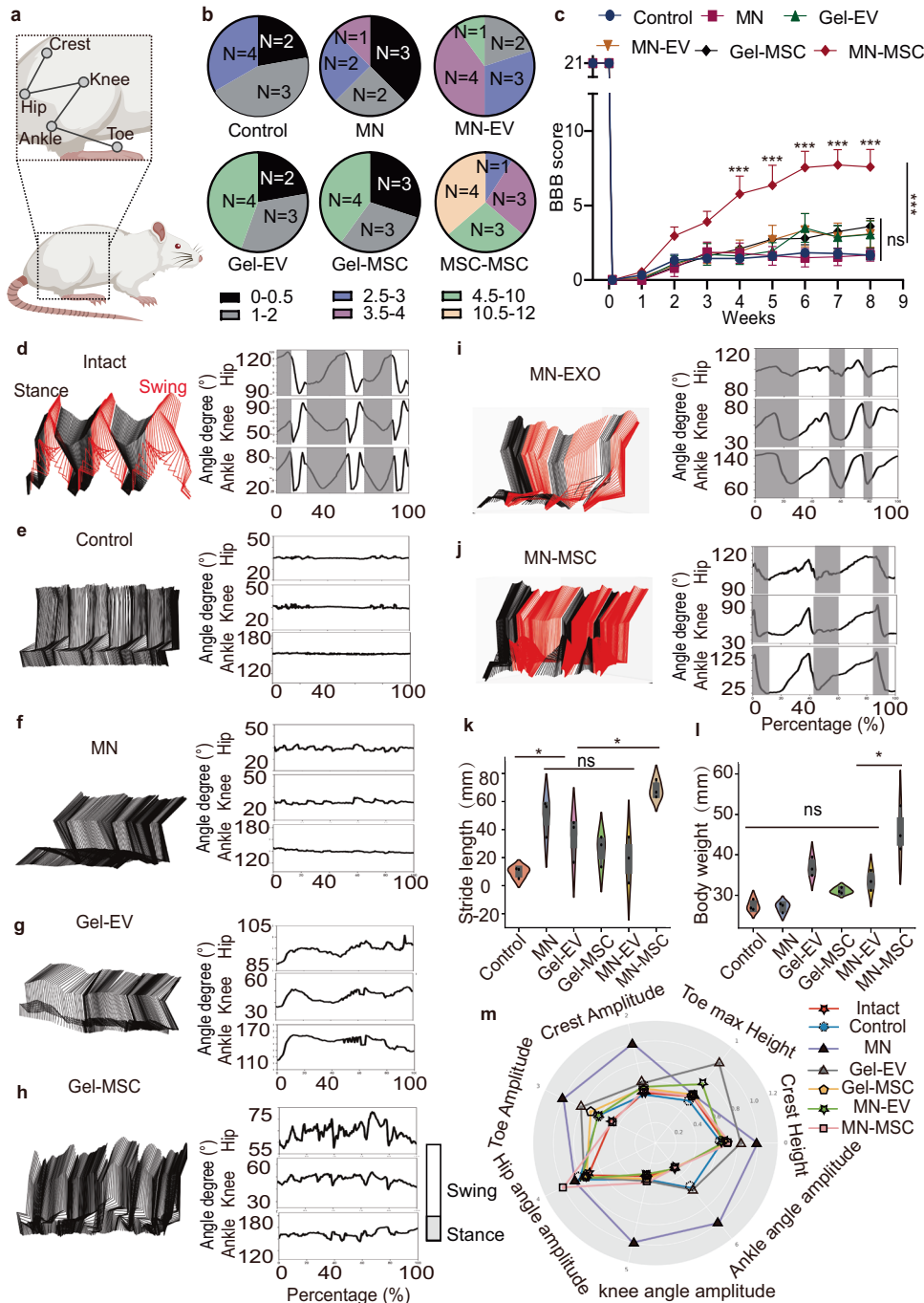


Fig. 6 | The hindlimb locomotor functional recovery of rats that underwent MN-MSC patch treatment after SCI. **a** Schematic illustration of hindlimb locomotor joint. **b** Distribution of BBB scores of rats in six treatment groups at 8 weeks after SCI. **c** Comparison of weekly BBB scores among rats in the six treatment groups at 8 weeks after SCI. Data are shown as the mean + SEM. Two-way ANOVA with Tukey's post-hoc test was used for comparisons among multiple groups, and two-tailed paired *t* tests were used for comparisons between two groups. Control: *n* = 9, MN: *n* = 8, Gel-EV: *n* = 9, Gel-MSC: *n* = 10, MN-EV: *n* = 10, MN-MSC: *n* = 11 independent animals. Total: *F* = 2.928, *p* < 0.0001. 4 weeks: MN-EV vs MN-MSC, *p* < 0.0001. 5 weeks: MN-EV vs MN-MSC, *p* < 0.0001. 4 weeks: MN-EV vs MN-MSC, *p* < 0.0001. 5 weeks: MN-EV vs MN-MSC, *p* = 0.0001. 6 weeks: MN-EV vs MN-MSC, *p* < 0.0001. 7 weeks: MN-EV vs MN-MSC, *p* < 0.0001. 8 weeks: MN-EV vs MN-MSC, *p* < 0.0001. **p* < 0.05, ***p* < 0.01, ****p* < 0.001. **d–j** Color-coded stick views and angle degree curves from intact (**d**), control (**e**), MN (**f**), Gel-EV (**g**), Gel-MSC (**h**), MN-EV (**i**),

and MN-MSC (**j**) groups. **k, l** Quantitative analysis of body strike length (**k**) and weight support (**l**). One-way ANOVA followed by Tukey's post-hoc test was used for comparisons among multiple groups and two-tailed paired *t* tests were used for comparisons between two groups. *n* = 3 independent animals. ANOVA for body strike length, Total: *F* = 9.771, *p* = 0.0007. Control vs MN, *p* = 0.0142, MN-EV vs MN-MSC, *p* = 0.0028. ANOVA for weight support, Total: *F* = 20.31, *p* < 0.0001, MN-EV vs MN-MSC, *p* = 0.0013. **p* < 0.05, ***p* < 0.01, ****p* < 0.001. The violin plot center indicates the median in all planes. Violin range covers 97.5th and 2.5th percentiles; extending whiskers show data distribution and probability density. Violin areas remain constant. Boxplot centerlines signify medians; boxes show first and third quartiles (Q1, Q3); whiskers extend from Q1 – 1.5xIQR to Q3 + 1.5xIQR; outliers lie outside whiskers. **m** Radar graph quantification of seven behavioral features of rats in the six treatment groups. For more details, see Fig. S10.

GelMA was mounted on the top of the MN patch before the blue light photocuring process was performed (Fig. 3a, S3a–i). As we know, the optimal time for suppressing acute SCI-triggered neuroinflammation and protecting the spared tissue/axons is within 7 days after SCI^{23,33}, so we dissected the spinal cord on the 7th day after SCI to assess whether MSCs survived in the MN-MS patch until this time point. As indicated by the images of spinal sections stained with hematoxylin and eosin (H&E) (Fig. 3d), the MN patch still persisted on the spinal cord surface at this time. More importantly, staining of the human MSC marker GAPDH in the spinal tissues indicated that the MSCs had survived well in the MN-MS patch on the 7th day after SCI (Fig. 3e, f, red). These results confirmed that the MSCs in the MN-MS patch can survive at the injury site long enough to cover the optimal therapeutic time window of SCI. Moreover, immunofluorescent staining of a serial spinal section from the spinal border to the center showed that MSCs from the MN-MS patch did not migrate from the GelMA hydrogel block into the spinal cord (Fig. S4). The results indicated that the fabricated device successfully maintained MSC viability, which may enable sustainable release of MSC-EVs for at least one weeks without MSC invasion into the spinal cord.

The MN-MS patch alleviates the inflammatory response in spinal cord lesions after SCI

To assess whether the MN-MS patch could ameliorate the SCI-induced neuroinflammatory environment, we constructed animal models without any treatment (control group), with MN patches implantation alone (MN group), with EVs in gel implantation alone (Gel-EVs group), with MSC in gel implantation alone (Gel-MS group), with MN patches embedded with MSC-EV implantation (MN-EV group) or with MN patches seeded with MSC implantation (MN-MS group) for comparison. 7 day after transplantation, we performed Western blotting analysis to detect the protein expression levels of the spinal tissues with spinal cord lesions in rats that underwent different treatments. In the spinal cord tissues of rats treated with the MN-MS patch, we observed a significant decrease in the expression of proinflammatory markers IL-1 β and TNF- α (Fig. 4a, b, g) and an increase in expression of the anti-inflammatory markers TGF- β and Arg-2 (Fig. 4a, d, h). Moreover, the expression of the proapoptotic marker BAX and the inflammatory marker MMP-9 was significantly reduced (Fig. 4a, e, f). Our experiments demonstrated that the MN alone exhibited some effect in reducing excessive TNF- α and MMP-9 expression (Fig. 4a, b, e), primarily controlled by M1 macrophages, compared to the control group (Fig. 4). All groups with the MN patch treatments exhibited decreased TNF- α and BAX expression, indicating suppressed inflammation. However, only the MN-MS treatment yielded a statistically significant increase in the anti-inflammatory cytokine TGF- β as well as increased arginase-2 and decreased IL-1 β expression. These findings suggest the beneficial effects observed could be partly attributable to a physiological reaction to the MN patch itself.

To further analyze the tissue-protective efficacy, sagittal sections of injured spinal cords at 8 weeks post-SCI were analyzed with immunofluorescence staining. Immunostaining for Iba1 (macrophages/microglia) showed significantly fewer activated immune cells in rats receiving the MN-MS patch treatment compared with control or MN-EV groups (Fig. S5a, e). In contrast, more neurons (NeuN) (Fig. S5b, f), blood vessels (CD31) (Fig. S5c, g), myelin (MBP) (Fig. S5d, h) and astrocytes (GFAP) (Fig. S5a–d, i) were observed in spinal tissues of the rats in the MN-MS group. Thus, evidence of cell preservation was only observed in the MN-MS treatment condition.

The MN-MS Patch Protects Spared Tissues/Axons from Secondary Injury

After verifying that MN-MS treatment could reduce SCI-triggered inflammation, we sought to assess whether this treatment could

protect spared tissues/axons from secondary injury after SCI. To determine whether more descending axons survived after being treated with an MN-MS patch, we injected AAV2/9-hSyn-mCherry into the T7-T8 region of the 6 groups of rats 2 weeks before sacrifice to trace the descending propriospinal axons (Fig. 5a). After staining the spinal sections with a red fluorescent protein (RFP) antibody (Fig. S6), we found no significant difference between numbers of RFP⁺ axons above the lesion site in the different treatment groups (Fig. 5d). However, rats in the MN-MS group had higher numbers of RFP⁺ propriospinal axons below the injury level compared to other groups (Fig. 5g).

Then, we stained the serotonergic axons and axonal fibers with anti-5-hydroxy tryptamine (5-HT) and anti-neurofilament (NF) in the spinal sections, respectively. We found that the trends of 5-HT and NF staining results were similar to that of RFP staining (Fig. 5, S7). No significant difference between NF and 5-HT was found above the injury site in the six groups (Fig. 5c, 3e, S7). In contrast, the rats in the MN-MS group had more serotonergic axons (stained by 5-HT) and axonal fibers (stained by NF) below the injury site than the rats in the other groups (Fig. 5f, 3h, S7), indicating that more propriospinal axons survived after SCI with MN-MS patch treatment. In contrast to the other groups, we found more axons that extended into the spinal cord lesion site in the examined subjects with MN-MS treatment (Fig. 5b and S7), suggesting that the microenvironment with the sustained EVs delivery from MN-MS patch treatment was more conducive to axon regrowth. In addition, we did not observe any significant difference between the control and MN groups in terms of protecting spared axons from secondary injury (Fig. 5, S6, S7). These results suggest that the microneedle arrays themselves did not have any effect on axonal protection. Interestingly, we did observe more 5-HT axons present beneath the injury in the rats with Gel-MS and Gel-EVs treatment compared with these with control, MN, Gel-EV treatments (Fig. 5b, f), suggesting these treatments exhibit some, albeit limited, neuroprotective effects. Remarkably, we observe a significantly higher number of axons situated beneath the injury site in the MN-MS group compared to the other groups (Fig. 5, S6, S7). These findings highlight the essential contribution of the microneedle patch to our treatment.

Recent studies on MSCs have reported that injecting MSCs directly into the vein (IV) or the damaged area (in situ) of the spinal cord can lead to some recovery in patients or animal models with SCI^{11,12,15}. To accurately compare the effectiveness of IV and local transplanted treatments, we conducted a study using both IV injection and in situ injection of MSCs alone as two additional controls. This allowed us to evaluate the ability of MN-MS to improve SCI under the same model and severity of injury (Fig. S8a). We found that the treatment with MSCs alone locally or through IV injection did not demonstrate any significant differences from the control group (Fig. S8b–d, S9).

The remnants of spared axons mediate hindlimb locomotor functional recovery

After verifying that more spared axons could be rescued by MN-MS patch treatment, we sought to determine whether these axons could mediate hindlimb locomotor functions. To this end, we analyzed the hindlimb performance of the rats with the Basso, Beattie, and Bresnahan (BBB) scale in a double-blind manner³⁴. We found that the rats in the other groups exhibited paralysis with occasional ankle movement during the observation period, with an average BBB score of less than 4 (Fig. 6c). Even though the rats in the MN-MS group predominantly demonstrated paralyzed hindlimbs during the first 3 weeks and showed no significant difference from the other groups (Fig. 6c), they showed vigorous knee and ankle movement at 4 weeks. The BBB scores of these rats were significantly higher than those of rats in the other groups at 4 weeks after injury. More strikingly, at the 8th week after SCI, the rats treated with the MN-MS patch showed improved hindlimb motor function, with higher body weight support and stride

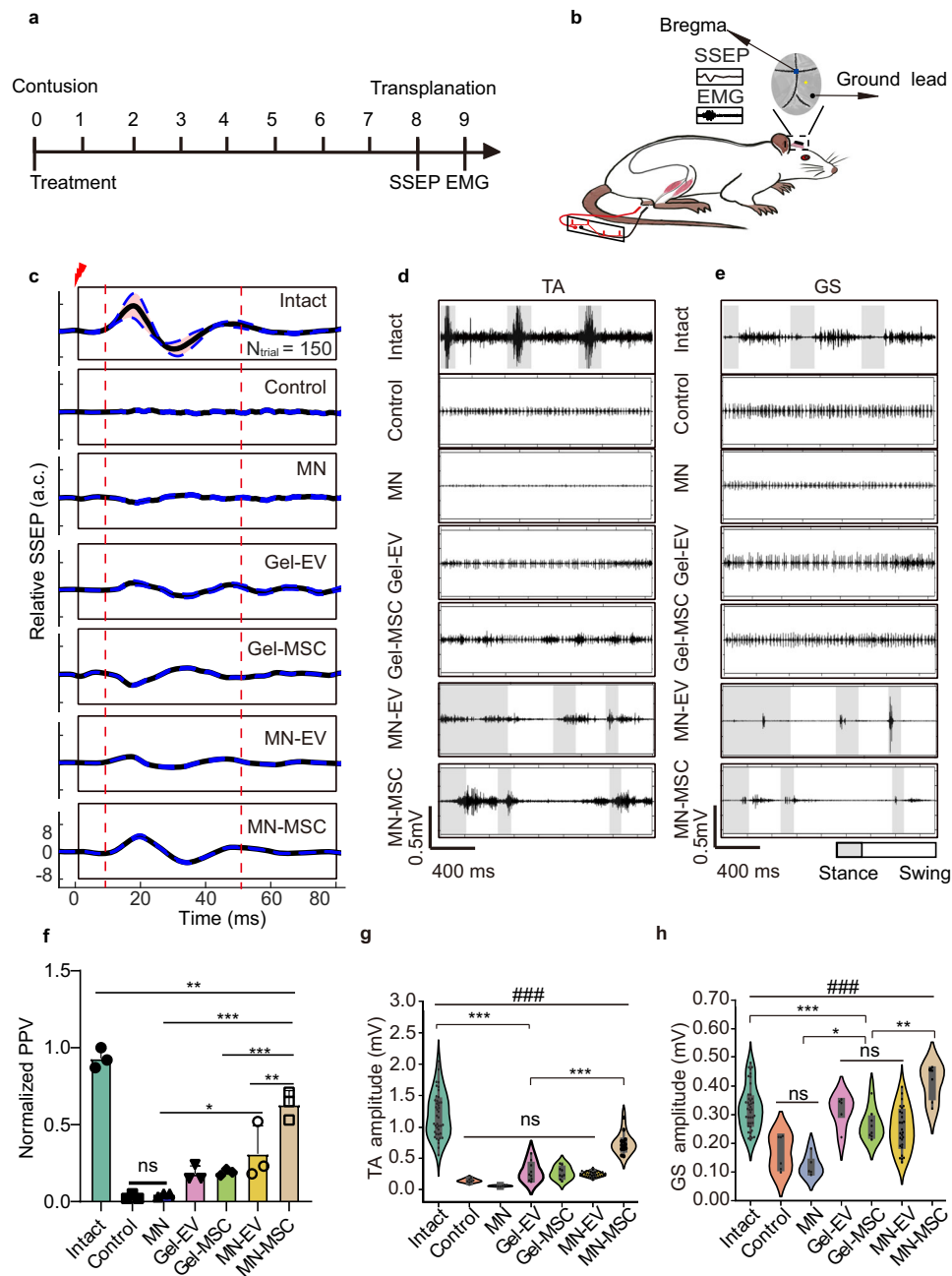


Fig. 7 | Electrophysiological recording experiments revealed the superior muscle control of rats treated with the MN-MSC patch. **a** Schematic diagram of the experimental design. **b** Schematic illustration of SEEP and EMG experiments. **c** Representative relative SSEPs of each group ($N_{\text{trial}} = 150$) are illustrated as the mean (solid line) and 95% confidence interval (shadow enveloped by a dashed line), and the time of electric stimulation was set to zero ms. **d, e** The representative TA(**d**) and GS(**e**) muscle EMG for rats of different groups. **f** Peak-to-peak potential was analyzed with one-way ANOVA followed by Tukey's post-hoc test. Two-tailed paired t tests were used for comparisons between two groups. Data are shown as the mean \pm SEM. $n = 3$ animals chosen randomly from each group. Total: $F = 46.59$, $p < 0.0001$, MN vs MN-EV, $p = 0.0221$, Intact vs MN-MSC, $p = 0.0092$, MN vs MN-MSC, $p < 0.0001$, Gel-MSC vs MN-MSC, $p = 0.0003$, MN-EV vs MN-MSC, $p = 0.0054$. * $p < 0.05$, ** $p < 0.01$, *** $p < 0.001$. **g, h** Quantitative analysis of signal amplitudes from TA(**g**) and GS(**h**) muscles for rats in different groups. One-way ANOVA with

Tukey's post-hoc test for comparisons among multiple groups (*) and two-tailed paired t tests were used for comparisons within groups (#) for the data shown in the violin plot. The violin plot center indicates the median in all planes. Violin range covers 97.5th and 2.5th percentiles; extending whiskers show data distribution and probability density. Violin areas remain constant. Boxplot centerlines signify medians; boxes show first and third quartiles (Q1, Q3); whiskers extend from Q1 – 1.5xIQR to Q3 + 1.5xIQR; outliers lie outside whiskers. Intact: $n_{\text{TA}} = 41$, $n_{\text{GS}} = 41$, control: $n_{\text{TA}} = 6$, $n_{\text{GS}} = 6$, MN: $n_{\text{TA}} = 6$, $n_{\text{GS}} = 5$, Gel-EV: $n_{\text{TA}} = 9$, $n_{\text{GS}} = 5$, Gel-MSC: $n_{\text{TA}} = 9$, $n_{\text{GS}} = 8$, MN-EV: $n_{\text{TA}} = 35$, $n_{\text{GS}} = 27$, and MN-MSC: $n_{\text{TA}} = 13$, $n_{\text{GS}} = 6$ trials for each group. ANOVA for TA: Total: $F = 78.441794$, $p = 8.507914 \times 10^{-38}$, Intact vs MN-EV, $p < 0.0001$. MN-EV vs MN-MSC, $p = 9.853309 \times 10^{-9}$. ANOVA for GS: Total: $F = 13.718067$, $p = 4.86509 \times 10^{-11}$. Intact vs MN-EV, $p = 8.533763 \times 10^{-4}$. MN vs MN-EV, $p = 4.474681 \times 10^{-3}$. MN-EV vs MN-MSC, $p = 4.238509 \times 10^{-5}$. *** p (or ### p) < 0.001 , ** p (or ## p) < 0.01 , * p (or # p) < 0.05 .

length than the rats in the other groups (Fig. 6k–i). Remarkably, we found that 4 of 11 rats in the MN-MS patch-treated group showed sustained weight support with hindpaw plantar stepping, and the BBB score reached more than 10, which was not observed in the rats in the other groups (Fig. 6b, Supplementary movie 1). Moreover, through subsequent analysis of the 7 kinds of hindlimb kinematics³⁵ of rats in the control, MN, Gel-EV, Gel-MS, MN-EV, MN-MS and intact groups, we found that the MN-MS patch treatment could increase the maximal height of the iliac crest and toe (Fig. S10a, b); the height amplitude of the iliac crest and toe (Fig. S10c, d). Interestingly, we observed an increased stride length in rats treated with MN, Gel-EV, Gel-MS, and Gel-EV compared to the control group, suggesting that the limited neuroprotective effects from MN may also contribute to their modest recovery (Fig. 6k). Meanwhile, in the Gel-EV, Gel-MS, and Gel-EV groups, the angle oscillation of the hip, knee, and ankle were larger than those in the MN group and comparable to the MN-MS group (Fig. S10e–g). However, the hindlimb locomotor performance of the rats treated with the MN-MS patch was significantly better than that of rats in the other groups but not as good as that of the rats in the intact group, suggesting that the hindlimb functional recovery with this treatment relied on the remnants of spinal connections across the lesion.

To take both features of data distribution and statistical meaning into account in each kinematics indicator, we drew a radar plot (Fig. 6m). While all indicators in each group were divided by the counterpart in the intact group, it was obvious that the amplitudes of the crest and toe of the rats in the MN-MS group were fairly high compared with those of rats in the other treatment groups (Fig. 6e–j). However, the maximum heights of the toe and crest of the rats treated with MN-MS were remarkably higher than those of rats in the other groups (Fig. 6m), possibly because the crest and toe determine the gait and stride length while walking. Upon comprehensively considering the values and distributions for each group, we found that angle amplitude changes at the ankles, knees and toes remained minimal in rats of the MN-MS group. This is consistent with results of the hindlimb kinematic analysis (Fig. S10).

To further determine the mechanism of action of the MN-MS patch treatment, we performed a somatosensory evoked potential (SSEP) monitoring study of the rats during anesthesia (Fig. 7b, c, f). Compared with the BBB score, SSEP is more direct for measuring the functionality of neuro pathways from cortical projections³³. As expected, we found that the SSEPs showed a similar trend to the BBB scores at the 8th-week post-injury (Fig. 7c, f), which confirms the axon protection capability of MN-MS patch treatment. Then, we recorded electromyography (EMG) data to assess the rats' hindlimb muscle motion when they were walking. We found that the ankle flexor signals of tibialis anterior (TA) muscles and extensor gastrocnemius soleus (GS) muscles were rarely active in rats in the control group, and the muscle signals of other treatment groups could only be occasionally observed. In contrast, alternating activation of the TA and GS for the MN-MS patch-treated rats could be consistently observed during different steps (Fig. 7d, e, g, h). To further analyze the EMG data, astronomical analysis (Poincaré statistical analysis) was used to analyze the rhythm of the TA and GS muscles³⁶. We found that the rhythms of TA and GS muscles of the rats in the MN-MS group were more regular than those of rats in the other groups with a wider distribution range of scatter points and more concentrated at the central points (zero) position, which were more similar to the one of the intact group (Fig. S11, S12), suggesting that those rats gain much better muscle control through MN-MS patch treatment. From this, we explored why the gaits of rats treated with MN-MS patches were closer to normal than the gaits of other rats. Together, these results suggest that improved locomotor function in the MN-MS patch treatment condition is mediated by axon rescue.

Discussion

In this study, we constructed an advanced MN-MS patch that can provide sustained delivery of MS-EVs from the MS-embedded patch to the spinal tissues in the injury site and avoid the risk of direct stem cells invading the spinal cord. The MN component of the patch was made of porous GelMA hydrogel with good biocompatibility, and the patch can remain on top of the spinal cord lesion for a long time, thus encompassing the optimal therapeutic window and achieving the maximum therapeutic efficacy of MS-EV treatment.

The study proposed an advanced MN-MS patch for SCI treatment, providing a platform for the long-term survival of MSs and enabling efficient and precise sustained delivery of MS-EVs to SCI lesions for an extended period, without direct invasion of MSs into the spinal cord microenvironment, thereby reducing the potential for additional damage from in situ transplantation. Traditional MS-EVs therapies were always hindered by the brief retention time of MS-EVs in living subjects^{9,22}. While, our data suggest that treatment with sustained MS-EVs by MN-MS patch after SCI could reduce secondary injury effectively^{10,15,33}. Previous studies have shown that MSs undergo apoptosis quickly when transplanted into the injury site in the presence of cytotoxic cells^{37–39}. However, in our MN patch, MSs are kept in a relatively moderated microenvironment after transplantation, and their ability to produce MS-EVs might be more stable, allowing them to exert a neuroprotective effect. MN-MS patches seeded with MSs provide an approach for achieving greater sustained delivery of MS-EVs for at least seven days after SCI than direct injection of MSs or MS-EVs. Furthermore, in this SCI model, MN-MS seeded patches effectively down regulated neuroinflammation after SCI, resulting in greater tissue sparing.

In this study, we double-blindly evaluated functional recovery in a model of severe contusive SCI. Our findings showed that MN-MS patch treatment could promote functional recovery by protecting the spared axons from secondary injury. Consistent with the MS secretome's function of immune modulation, apoptosis inhibition^{17,40} and enhanced angiogenesis^{20,41,42}, greater vascularization (CD31) formed in the spinal cord lesion of SCI rats with our treatment. Such vessels can supply sufficient nutrients and oxygen to remodel the SCI microenvironment and then protect spared axons^{15,33,43}. Furthermore, the spinal cord of rats treated with the MN-MS patch showed less inflammation (Iba1, TNF- α , IL-1 β , MMP-9) and more anti-inflammatory factors (TGF- β , Arg-2) with more neurons (NeuN), less apoptosis and death of spinal cord cells (BAX), and more myelin sheath (MBP), which benefit the plasticity of spinal circuitry in terms of function. While some groups with the MN patch also benefitted by modulating the excessive immune response, this effect could be attributable to the inherent properties of GelMA in regulating the neuroinflammatory microenvironment. No significant differences were observed between the Gel-EVs and MN groups, potentially due to the limited therapeutic effects of Gel-EVs (Fig. 4a, b, e). Furthermore, the Gel-MS and MN-EV groups demonstrated enhanced immunosuppression by decreasing TNF- α levels compared to the MN groups (Fig. 4a, e). These results suggest the MN-MS treatment shifts the pro-inflammatory and anti-inflammatory balance from an M1 macrophage-dominant state (as in control groups) to an M2 macrophage-dominant state²², possibly due to sustained MS-EVs delivery by the MN-MS patch. These findings highlight the need for both microneedles to enable effective delivery and MSs to achieve sustained MS-EVs delivery, thereby accomplishing reliable immunomodulation.

Additionally, by axon tracing and labeling, we showed that more axons survived secondary injury by MN-MS patch treatment. In comparison with the rats in the control or other treatment groups, the rats with MN-MS patch treatment exhibited remarkable hindlimb locomotion functional recovery, which is consistent with their better muscle control ability, as indicated by the PPV and signal of TA and GS muscle EMG recording studies. However, a variety of functional recovery levels

was observed in the rats treated by MN-MS patches, possibly because the rescued axons that are closely relevant to hindlimb locomotion were randomly presented in the treated rats. The therapeutic effects observed in this study may be explained by the effective vascularization (Fig. S5) and inflammatory mitigation (Fig. 4) elicited by the MSC-EVs.

Although MSCs release many soluble proteins in addition to EVs, preliminary studies with a small number of animals found that the addition of GW4869⁴⁴ (which block exosome release) to the MN-MS patch blocked the histological and functional improvements observed with MN-MS patches without GW4869 (Fig. S14). This implies that release of EVs from the implanted MSCs may be necessary for the therapeutic effects. However, we cannot rule out the possibility that tropic factors or other soluble molecules might contribute to the effects. Additionally, we cannot exclude the possibility that these factors coexist and synergize with the generation of MSC-EVs^{45–47}. The interplay between MSC-EVs and other factors, such as trophic factors, remains one of the main challenges in the MSC therapy field and awaits further investigation^{10,15}. Our findings indicate that the sustained release of EVs is crucial, but we cannot exclude the possibility that other factors, such as releasing a greater total number of EVs or delayed release, may also contribute to the observed therapeutic effects of the MN-MS patch. Other strategies are needed to better preserve transplanted MSCs' stemness, thereby improving treatment efficacy. These remain the limitations of this study.

While we have demonstrated the proof-of-concept for the MN-MS patch in SCI treatment, the optimal time window for MN-MS patch implantation remains to be determined. In an additional experiment, MN-MS patch implantation was performed on the 3rd, 7th, and 14th days following contusive SCI. Associated data shows that the application of the MN-MS patch at 3 hr, 3 days, or 7 days post-SCI resulted in axon sparing below the lesion and improved locomotor recovery, but that treatment at 14 days did not do either (Fig. S13). The proposed MN-MS transplantation treatment is likely effective within at least the first week after SCI, in line with previous studies indicating that the optimal transplantation time window for neuroprotective treatments falls within the first week post-SCI^{10,16,34}. Moreover, in contrast to the MN-MS treatment conditions, in our hands, IV infusion or direct transplantation of 1.0×10^6 MSCs one week post-injury failed to produce statistically significant improvements in locomotor recovery or axon sparing (Fig. S8), arguing that the MN scaffold may provide for superior survival and engraftment of MSCs. However, optimizing treatment timing requires further investigation.

Since the MN-MS patch was fabricated from GelMA hydrogel, we envisioned that the MN-MS patch would degrade in the long term^{29,48}. However, whether the materials of the MN-MS patch could completely degrade should be investigated in future studies. In addition, the relationship between the number of EVs released from the MN-MS patch and the best treatment efficacy has not been tested and therefore needs to be investigated before clinical study. While our study demonstrated that MN-MS transplantation was effective within the first week following SCI, further optimization of the transplantation time window may be necessary for pre-clinical exploration. To promote diffusion and improve delivery efficiency, in our next step, we plan to construct a precise porous MN structure at the micro/nano scale with two-photon 3D printing technology, which might have higher precision in controlling the porous size of the MNs⁴⁹. Moreover, the MN-MS patch might be too soft to be used as an artificial dura for clinical SCI treatment, and a tenacious MN-MS patch with the addition of a scaffold structure between the MN array and the MSC-embedded patch is being developed by our group.

Methods

Materials

Chicken anti-GFAP [abcam (ab134436, 1:500)], GAPDH (Human Specific) Rabbit mAb [Abclonal (AC036), 1:500], rabbit anti-neurofilament

(NF) heavy polypeptide [abcam (ab8135), 1:500], goat anti 5-HT antibody [abcam (ab66047), 1:500], rabbit anti-NeuN [abcam (ab177487), 1:1000], Rabbit polyclonal to RFP [abcam (ab62341), 1:500] rabbit anti-MBP [abcam (ab218011), 1:500], goat anti-IBA1 [abcam(ab5076), 1:500] rabbit anti-CD31 [R&Drd system (AF3628), 1:500], GAPDH Rabbit Monoclonal Antibody [Beyotime (AF1186,1:1000)] rabbit anti-TGF- β [Abclonal(A2124), 1:1000], rabbit anti-Bax [Abclonal (A0207),1:1000], rabbit anti-MMP9 [Abclonal (A0289), 1:1000], rabbit anti-Arginase 2 (ARG2) [Abclonal (A19233), 1:1000], Donkey anti-Chicken IgY H&L (FITC) [Abcam (ab63507), 1:500], Donkey anti-Rabbit IgG H&L (Alexa Fluor® 555) [Abcam (ab150062), 1:500], Rabbit anti-Goat IgG H&L (Alexa Fluor® 555) [Abcam (ab150142), 1:500], Donkey anti-Rabbit secondary antibodies (HRP) [beyotime (A0208), 1:1000], Rabbit anti-iNOS [proteintech (80517-1-RR), 1:2000] Rabbit anti-TNF- α [proteintech (17590-1-AP), 1:1000], Rabbit anti-IL-1 β [Abclonal (A20527), 1:1000] Rabbit α -Tubulin [beyotime (AG0126), 1:1000] were used. PE Mouse anti-Human CD105 [BD Pharmingen™, 560839,1:20], APC Mouse Anti-Human CD90 [BD Pharmingen™, 561971, 1:20], PE Mouse Anti-Human CD73 [BD Pharmingen™, 550257, 1:20], FITC Mouse Anti-Human CD45 [BD Pharmingen™, 561865, 1:20], FITC Mouse Anti-Human CD34 [BD Pharmingen™, 560942, 1:20], APC Mouse Anti-Human CD19 [BD Pharmingen™, 561742, 1:20], APC Mouse Anti-Human CD14 [BD Pharmingen™,555399, 1:20], PE Mouse Anti-Human CD11b [BD Pharmingen™, 555388, 1:20], PE Mouse Anti-Human CD79a [BD Pharmingen™, 561942, 1:20], PE Mouse Anti-Human HLA-DR [BD Pharmingen™, 555812, 1:20] were used. The adenovirus-associated virus AAV2/9-hSyn-mCherry was generated by the viral core of Zhejiang University, and its titer was adjusted to 1×10^{13} copies per mL for injection. DAPI-containing antifade mounting medium was purchased from Southern Biotech (0100-20, USA). Triton X-100 (PI080) was purchased from Solarbio (China). Lithiumphenyl-2, 4, 6-trimethylbenzoylphosphinate (LAP), polydimethylsiloxane molds (EFL-MMN-600), traditional GelMA (EFL-GM-PR-001) and porous GelMA (EFL-GM-PR-001) were purchased from EFL Inc. (Suzhou, China). GW4869 were obtained from the Sigma-Aldrich. Serum-free medium for MSCs (NC0103 + NC0103, S, Yocon, Beijing, China). Serum-free medium for MSCs and stem cells moderate digestive enzymes were bought from Yocon. CCK-8 assay was bought from Dojindo. Live/dead viability/cytotoxicity kit was bought from Invitrogen. CM-Dil was bought from Yeasen.

Animals

Female Sprague–Dawley rats (220–250 g) were purchased from the Zhejiang Academy of Medical Sciences. All animal experiments were approved by the Institutional Animal Care and used following the provisions of Zhejiang University Animal Experimentation Committee and Independent Ethics Committee (ZJU202010110). The rats were housed under controlled environmental conditions and were completely in compliance with the National Institutes of Health Guide for the Care and Use of Laboratory Animals. The implantation of electrodes was performed under anesthesia with dexmedetomidine hydrochloride (0.25 mg/kg i.p.; MCE, US) and 0.5% isoflurane. All the other surgeries were performed under anesthesia with 1% (w/v) pentobarbital sodium (5 mL/kg, injected intraperitoneally).

Preparation of MSC

Human embryonic stem cell (ESC)-derived MSCs were generated by Ysbiotech, Hangzhou, China (YS™ hESC-MSC) and cultured at 37 °C in a humidified atmosphere of 5% CO₂ in serum-free medium for MSCs (NC0103 + NC0103, S, Yocon, Beijing, China) as previously reported⁵⁰, with some modification. The H9 human embryonic stem cell line (WA09), originally generated by the National Stem Cell Bank c/o WiCell Research Institute (USA), was obtained from the stem cell bank at the Institute of Biochemistry and Cell Biology, CAS. ESC-MSCs were differentiated from ESC as following the method. Briefly, the H9-ESC

colonies were dissociated into small clumps using TrypLE Express and cultured in ultralow-attachment plates with E8 medium (Gibco, Grand Island, NY, USA). After one week, we harvested the embryoid bodies and cultured them in MSC induction medium (high-glucose Dulbecco's modified Eagle's medium, 10% fetal bovine serum, and 1 mM L-glutamine). After 15 days, the outgrowths of embryoid bodies were sub-cultured using TrypLE Express, yielding MSCs designated as passage 0. The MSCs were subsequently cultured in serum-free medium. When the proliferating colonies had reached near confluence, the hESC-MSCs were passaged using stem cells moderate digestive enzymes (NC1004, Yocon, Beijing, China). After 4 passages, MSCs were used for transplantation or other investigations.

To confirm the MSC phenotype of the obtained cells, we analyzed their CD immuno-profile using flow cytometry (the flow cytometric gating strategy see Fig. S15–17). Specifically, we used flow cytometry to assess the expression of CD73, CD90, CD105, CD45, CD34, CD19, CD14, CD11b, CD79a, and HLA-DR to make sure their MSC phenotypes (results see Fig. S1, CD73⁺, CD90⁺, CD105⁺, CD45⁻, CD34⁻, CD19⁻, CD14⁻, CD11b⁻, CD79a⁻, and HLA-DR⁻)^{38,50}.

Preparation of Extracellular Vesicles

We employed a modified differential centrifugation method to isolate extracellular vesicles from MSCs⁵¹. Briefly, when the MSCs reached 80–90% confluence, we washed them with PBS and added complete medium containing exosome-free medium for 48 h. The supernatant was collected and subjected to centrifugation at 350 *g* for 15 min and 2300 *g* for 20 min at 4 °C to remove cells and cellular fragments. After filtration through a 0.22 μm filter, the medium was ultra-centrifuged at 120,000 *g* for an additional 2 h at 4 °C to collect MSC extracellular vesicles. The vesicles were then resuspended in 100 μL of sterile PBS. We analyzed the size and morphology of the extracellular vesicles using transmission electron microscopy (TEM) with a JEM-1400 flash microscope (JEOL, Japan). We quantified the extracellular vesicles using nanoparticle tracking analysis (Marvin, UK, Nanosight NS500). Specifically, we first diluted the obtained solution suspended in PBS (approximately 2 μg/μL) by 100-fold and then analyzed it based on light scattering using an optical microscope aligned perpendicularly to the beam axis. Finally, we quantified the vesicles using NTA software.

Fabrication and characterization of MN arrays

The MN arrays were fabricated with polydimethylsiloxane molds. GelMA (EFL-GM-60) and porous GelMA (EFL-GM-PR-001) were used to create traditional MN arrays and porous MN arrays, respectively. The traditional GelMA (EFL-GM-60) comprises Gelatin methacryloyl (GelMA, Mw ~150 kDa, degree of substitution: 60%) and lithiumphenyl-2, 4, 6-trimethylbenzoylphosphinate (LAP) in a mass ratio of 100/5. The porous GelMA (EFL-GM-PR-001) consists of GelMA (Mw 150 kDa, degree of substitution: 60%), polyethylene oxide (Mw = 300 kDa), and photo-initiator LAP in a mass ratio of 100/15/5. 5% (w/v) solution of EFL-GM-60/ EFL-GM-PR-001 were selected to fabricate the Microneedles array according to previous report^{29,30}. To create the MN arrays, we first prepared a 5% (w/v) solution of either traditional GelMA or porous GelMA at 37 °C and dispensed it into molds. Next, the bubbles of the casting solution were removed by vacuum pumping, and the molds were placed in a 37 °C environment for 10 h to dry. Then, the casting solution was solidified with blue light curing (405 nm, 30 mW/cm²) for 30 s. After that, the MN was separated from the molds with tweezers cautiously. The MNs had diameters of 250 μm, which tapers for a height of 600 μm. The MN arrays were arranged 550 μm, tip to tip, in a 4 mm × 4 mm area. The morphology of the MNs was assessed with a SEM (Nova Nano 450, Thermo FEI, USA).

The compressive mechanical properties of the dry traditional GelMA and porous GelMA gel scaffolds were tested using a texture analyzer (Stable microsystem, TA-XTPLUS, UK). Prior to testing, the samples were soaked in PBS for 4 h. The preload was set to 0.1 N and

the maximum compression strain was set to 80%. The stress-strain curve was obtained, and the compression modulus of the sample was calculated based on the slope of the curves in the range of 0–30% deformation. Three samples were tested in each group. The mechanical properties of the MN were tested using a universal testing machine (CMT5205, MTS, China). The MN patches were placed on the test bench with the tip of the needles facing upwards. The compress parameter was set to 0.005 mm/s, and the measured force and displacement were recorded. Three samples were tested in each group.

Fabrication of the MN-MSC, MN-EV patch, Gel-EV and Gel-MSC

First, the MSCs were digested by stem cell digestive enzymes and evenly mixed into a 5% (w/v) porous GelMA solution with final concentration of about 2.5×10^7 cells/mL at 37 °C. Next, the 40 μL solution with MSCs (totally about 1×10^6 cells) was added to the basal side of the MN arrays¹⁶. After a 30 s blue light curing process, the MN-MSC patch was obtained. The MN-MSC patch was cultured in MSC serum-free media for in vitro and in vivo testing. According to previous reports²², we estimated that 1×10^6 cells could secrete approximately 1.68×10^{10} EV particles within the first week post-transplantation. Consequently, a roughly equivalent amount of MSC-EVs to the number of EVs secreted by MSCs was mixed into a 5% (w/v) porous GelMA solution, resulting in a final concentration of approximately 4.2×10^{11} particles/mL. Next, the 40 μL solution with EVs (totally 1.68×10^{10} EVs) was added to the basal side of the MN arrays at 37 °C. After a 30 s blue light curing process, the MN-MSC patch was obtained. The MN-MSC patch was cultured in MSC serum-free media for in vitro testing.

Gel-EVs were fabricated by direct photocuring a 5% (w/v) porous GelMA mixed MSC-EVs solution (40 μL solution, 1.68×10^{10} EVs) and Gel-MSCs fabricated by direct photocuring a 5% (w/v) porous GelMA mixed MSCs solution (40 μL solution, 1×10^6 cells).

MSCs viability analysis in porous MN-MSC Patch

The viability of MSCs in the MN-MSC patch was evaluated with a live/dead viability/cytotoxicity kit (L3224, Invitrogen, USA). After washing the MN-MSC patch with phosphate-buffered saline (PBS) for three times, the MSCs were stained with 0.2% ethidium homodimer-1 (EthD) and 0.05% Calcein AM in PBS for 20 min. Then, the MN-MSC patch was washed with PBS for three times and observed by laser scanning confocal microscopy (Nikon, AIR). The proliferation of the MSCs in the MN-MSC patch was tested by CCK-8 assay (CK04, Dojindo, Japan) on the 1st, 3rd and 5th days. And the optical density of formazan was detected at a wavelength of 450 nm by a microplate reader (iD5, Molecular Devices, USA). To quantify the in vivo viability of MSCs in the porous MN-MSC patch, we implanted the MN-MSC patch in the injured spinal cord of rats using the surgical procedure described in the Animal and Surgical Procedures section. After implantation, we obtained images of the MSCs in the spinal cord injury site by H&E staining and immunofluorescence staining for GFAP/DAPI/hGAPDH. The images were acquired using a slide scanner (VS200, Olympus, Japan).

Release and delivery analysis of the MN Patch

To compare the MSC secretome release capacity of MN-MSC patches fabricated with porous and traditional GelMA hydrogels, the amount of protein released from the patches was analyzed. Briefly, the porous MN-MSC patch and normal patch were stabilized in Transwells⁵², respectively (Fig. 4i). Next, the patches in 24-well plates containing MSC were cultured in serum-free media at 37 °C for two weeks, and the medium from the Transwell bottom was collected once every two days. The released proteins in the culture medium were quantified using a Micro BCA Protein Assay kit⁵³. All release experiments were repeated three times for consistency and reliability of the results.

To evaluate the EV release capacity of the MN-MSC patch and MN-EV patch, we used a Transwell setup to simulate in vivo release (Fig. 2i).

The immobilized patches were cultured in MSC serum-free media at 37 °C for two weeks, and we collected the medium from the Transwell bottom every two days. The released EVs were isolated from the collected medium using the differential centrifugation method described above and quantified by NTA (Marvin, UK, Nanosight NSS00). We repeated each release experiment three times to ensure reliability and consistency of the results.

To quantify the EV delivery capacity of the MN patches, we used CM-Dil-labeled EVs (2 mg·mL⁻¹, Yeasen, China) (CM-Dil-MN-EV) as a representative of the EVs released by MSCs. We implanted the CM-Dil-MN-EV patch in the injured spinal cord of rats using the surgical procedure described in the Animal and Surgical Procedures section. We obtained images of the stained EVs released in the spinal cord injury using a slide scanner (VS200, Olympus, Japan).

Surgical Procedure

For *in vivo* experiments, a spinal contusion injury model was induced by an infinite vertical impactor (68099, RWD, China). To facilitate surgical procedures, we performed anesthesia for the contusive injury and transplantations using 1% (w/v) pentobarbital sodium following a well-established protocol to minimize rat mortality. Specifically, after being anesthetized, a laminectomy was performed at the tenth thoracic vertebral level (T10-II) of a rat to expose the dorsal surface to induce SCI. Next, contusion was performed using a cylinder (diameter, 3 mm) that impacted the spinal cord at a rate of 2.5 m/s and was left for 5 s at a depth of 2 mm after being impacted (Fig. S3b, c). To ensure blinding of the treatment conditions, a skilled technician who was independent and unaware of the treatment performed the implantation surgeries.

All implantation surgeries were performed by a technician who was blinded to the transplantation materials. An independent technician was responsible for randomly assigning rats, maintain treatment records, and label animals without involvement in the surgery. The implantation procedure involved three steps. First, the dura mater at the lesion site was cut carefully using a pair of microscissors (S11001-09, RWD, China) in the direction of the spinal cord. The second step is implanting. For MN, MN-EV, and MN-MSC group, the MN was placed at the site of the dura matter defect. 40 µL porous GelMA (5% (w/v)) (MN group) or GelMA (5% (w/v) contains 1.68 × 10¹⁰ particles EVs(MN-EV group) or MSCs (25,000 cells/µL, 1 × 10⁶ cells, MN-MSCs group) were dripped onto the MN and irradiated with light at a wavelength of 405 nm for 1 min to create the patches (Fig. S3f). For Gel-EV and Gel-MSC group, the prepared Gel-MSC, Gel-EVs, were directly implanted on the site of the dura matter defect separately. For the MSC-Local group, MSCs were injected into the lesion (20 µL solution containing 1 × 10⁶ cells in PBS for each rat). Third, 5% (w/v) porous GelMA solution was added onto the surface of the exposed spinal cord with the patch and gelled with blue light to secure the patch on the spinal cord injury site (Fig. S3g–i). The control group and MSC-IV group rats underwent contusion and dura mater cutting without placement of any material. The MSC-IV group rats received a total of 1 × 10⁶ MSC injections at 3 day post-SCI following a reported protocol¹⁶. Additionally, MN-MSC group transplanted were conducted as the same method at 3, 7, 14 days after SCI. Moreover, MN-MSC + GW4689 group transplanted were conducted using the same method, but the 5% (w/v) porous GelMA containing GW4689 solution (20 µM)⁴⁴. All rats were carefully sutured and labeled. Antibiotics (Baytril, 10 mg/kg) and painkillers (buprenorphine, 0.05 mg/kg) were administered to the animals for the first two weeks to ensure their well-being. The rats did not receive any immunosuppressive medication. Artificial micturition was performed twice daily until automatic bladder voiding was restored. To maintain surgical quality, no more than 15 rats were operated on per day.

At 6 weeks after injury, anterograde tracing of propriospinal axons was performed via the injection of AAV2/9-hSyn-mCherry at the T7-8 spinal cord by independent technician^{33,35}. Specifically, a pull-glass micropipette tipped with a 10-µL Hamilton microsyringe (68606, RWD, China) was used for precise injection. After a laminectomy was performed at the T7-8 spinal cord, AAV2/9-hSyn-mCherry was injected into 12 sites at the following locations: (1) 0.4 and 0.8 mm lateral to the midline; (2) 0.5, 1.0 and 1.6 mm from the surface. The injection rate was 80 nl/min, and the injected liquid volume was 150 nl per site. The needle was left for 1 min before moving to the next. Animals were sacrificed for assessment 2 weeks after injection.

Western blotting

At the post-SCI 7day, rats were randomized selected to assess their immunity. Another group of examiners blinded to the treatment groups processed the western blotting. Tissues were washed three times with ice-cold PBS and lysed in RIPA buffer containing 1% PMSF. After leaving the samples on ice for 30 min, they were centrifuged at 12,000g for 15 min at 4 °C. Protein concentrations in the supernatant were assessed using a Micro BCA Protein Assay kit. Equal amounts of protein extracts were resolved by 10–12% SDS-PAGE and electrotransferred onto a polyvinylidene membrane (Bio-Rad, USA). After blocking in Tris-buffered saline plus 5% (w/v) milk, the membranes were exposed to primary antibodies overnight at 4 °C. The samples were incubated with secondary antibodies conjugated to horseradish peroxidase for 1 h at room temperature. An independent examiner blinded to the treatment groups assessed these gene expressions. Signals were visualized by a ChemiDoc Touch Imaging System (Bio-Rad, USA), and ImageJ software was used to assess their average inflorescence intensity. All experiments were repeated three times.

Implantation of electrodes

Electrode implantation was performed 8 weeks after SCI for both evoked potential and hindlimb EMG according to previously published protocols³³. To minimize the effect on evoked potential recordings, we anesthetized the rats with dexmedetomidine hydrochloride (0.25 mg/kg *i.p.*; MCE, US) and 0.5% isoflurane⁵⁴. A stainless steel screw electrode (the yellow star in Fig. 7b) was fixed on the skull above the hindlimb region stereotactically (Behind: -2.0 mm/ Right: +2.5 mm/ Deep: -0.7 mm compared with bregma (blue triangular in Fig. 7b)) for an epidural recording of cortical evoked potentials referring to the zero potential on the shoulder (ground lead (black circular in Fig. 7b)) connected to Behind: -6.0 mm/Right: 4.0 mm compared with bregma⁵⁵. Following the SSEP recording, bipolar electrodes (AS632, Conner wire) were inserted into the right medium gastrocnemius (GS) and TA for *in vivo* assessment of hindlimb muscles with the reference lead linked to the ipsilateral tendon³³. Wires were subcutaneously connected to the header plate fixed on the skull. Electrode implantation was operated by an independent examiner blinded to the treatment groups.

SSEP recording and processing

During the surgery, the header was connected to a neuron signal amplifier (BTAM01L, Braintech, China), and the signal was recorded by an independent examiner with a NeuroStudio system (Braintech, China)⁴⁷. A series of pulses (2.0 Hz, 2.0 mA, 0.5 ms) was applied to the left hindlimb paw through a pair of electrodes by a neurostimulator (BTSEM-16, Braintech, China) under anesthesia³³. Signals were obtained from a 5-min stimulation, followed by a 30- to 1500-Hz bandpass, power line noise notch filtration (50 Hz and the two consequent harmonics 100 Hz and 150 Hz), and the removal of stimulation artifacts. Then, the first 150 qualified trials were chosen for peak-to-peak potential (PPV) calculation. The PPV was normalized according to

the intact group, following the method described by Gunnar Waterstraat et al.⁵⁶.

EMG recording and processing

Seven days post-implantation, five osteoarticular structures were captured to distinguish stance and swing when moving freely, and the header was connected up to the amplifier to detect muscle strength. Next, the free-moving muscle activity, represented by an extensor and a flexor of the right hindlimb, was logged in NeuroStudio. Data were filtered (bandpass 20 Hz–1000 Hz) before computing the muscle amplitude on the MATLAB platform⁵⁷. The EMG Recording and Processing were by technicians blinded to the treatment groups. In this study, we employed the Poincaré analysis method to differentiate chaos from randomness by embedding datasets into a higher-dimensional state space. For instance, a time series of EMG peak signals was represented as follows:

$$x_t, x_{(t+1)}, x_{(t+2)}, \dots, x_{(t+n)}$$

To generate a return map in its simplest form, we plotted $(x_t, x_{(t+1)})$, $(x_{(t+1)}, x_{(t+2)})$, and then $(x_{(t+2)}, x_{(t+3)})$, and so forth. x_t is the signal value of the electromyographic signal x at time t , where $t = 1, 2, \dots, t + n$ are time points separated by n time intervals from time t , where $n = 1, 2, \dots$. This approach allowed for a clear representation of the interval length between two EMG peak signals in a series, enabling rhythm quantification across different groups (Intact, control, MN, Gel-EV, Gel-MSc, MN-EV, and MN-MSc). Ultimately, we obtained both amplitude and rhythm information by analyzing the EMG data. In the Poincaré plot, healthy individuals are represented by a flatter ellipse, whereas unhealthy individuals exhibit a larger length-to-width ratio, resulting in a wider ellipse in the Poincaré plot.

Histology

Animals were sacrificed at 8 weeks after injury for histological assessment. Independent examiners who were blinded to the treatment groups processed the spinal cord tissue and stained the slides. After the animals were anesthetized, perfusion was performed using PBS and 4% paraformaldehyde. Spinal cords and other tissues were fixed in 4% paraformaldehyde overnight and dehydrated with sucrose for 1 day. And the fixed tissues were dehydrated in 15 and 30% sucrose solutions. After being embedded using optimal cutting temperature compound (OCT), twenty-micrometer-thick sections of the spinal cord were cut using a cryostat (CryoStar NX50; Thermo, USA) and mounted onto slides. For sagittal continuous section analysis, we randomly selected several 8 mm long midsagittal sections which containing the epicenter of injury. And the examined sagittal sections of spinal cords were from the same level (T9–T11). For coronal section analysis, we selected rostral and caudal tissue from the region adjacent to the sagittal tissue. For immunofluorescence histochemistry, spinal cord tissue sections were blocked with 5% donkey serum and 0.3% Triton X-100 for 1 h and incubated with primary antibodies overnight at 4 °C. After washing with PBS three times, the tissues were incubated with secondary antibodies conjugated to fluorescent dyes for 2 h at room temperature. Then, tissues were rewashed with PBS and dripped with an antifade mounting medium containing DAPI. The sagittal serial sections were stained with 5-HT (serotonergic axons), RFP (propriospinal axons), NF (axonal fibers), GFAP (Astrocyte), NeuN (neurons), MBP (myelin sheath), CD31 (blood vessels), and Iba1 (microglia). The coronal serial sections were stained with 5-HT, RFP, and NF. Whole images were acquired using a slide scanner (VS200, Olympus, Japan) and for enlarged details, images were acquired using a confocal laser scanning microscope (A1Ti, Nikon, Japan). For the same staining images, all groups use the same imaging parameter. An independent technician who was blinded to the

treatment group used the same region of interest to quantify fluorescent staining for these images. Specifically, the spared axons were quantified by their average fluorescence intensity in rostral and caudal sections, while microglia were quantified by Iba1 immunoreactivity average fluorescence intensity in sagittal sections. The area of other tissues, including those marked by GFAP, NeuN, MBP, and CD31, were quantified by their ratio to the total spinal cord area marked by DAPI in sagittal sections. At least three sections apart 40 μm were chosen for each spinal cord. All images adjust and fluorescence intensity quantification was using ImageJ software. After collecting all the data, the technician responsible for recording the treatments and animal tags divided the rats into different groups. The data from 3–5 animals were analyzed and organized into figures using Graphpad software.

Some spinal cord tissue and organ sections were stained with hematoxylin and eosin H&E. Images were acquired by a slide scanner (VS200, Olympus, Japan). For hematoxylin and eosin staining, spinal cord tissue and organ sections were hydrated in deionized water (DI) and left in hematoxylin for 5 min. The samples went through a series of washes and left in Eosin Y for 1 min and 20 s. The samples went through another series of ethanol washes and analyzed using slide scanner (VS200, Olympus, Japan).

Behavioral assessment

The locomotion performance of the rats was recorded by an independent examiner with a camera once a week during the experiments. Another examiner blinded to the treatment assessed the videos recording the rats' behavioral performance by the Basso, Beattie Bresnahan rating scale (BBB scale)³⁴. Rats that showed a BBB score above 1.5 at 1 week after SCI were excluded from further histological or behavioral analysis. To precisely understand the locomotor kinematics, the representative hindlimb osteoarticular landmarks (toe, ankle, knee, hip, and crest) were labeled by 5 mm reflective balls and tracked by the MotoRater (Vicon Nexus, UK)³³. Typical sequential treads and the ankle degrees of selected articulates were displayed. Body weight support and stride length were compared as previously described³⁵.

The behavioral data were depicted with seven features (maximal iliac crest height; crest height amplitude; maximal toe height; toe height amplitude; and hip, knee and ankle angle oscillation) within four groups (intact, control, MN, Gel-EV, Gel-MSc, MN-EV, and MN-MSc). For each group, we utilized different statistical methods to evaluate the seven behavioral features, and these features have different units. As we needed to thoroughly analyze these features in radar graphs, normalizing these data was vital and pivotal. First and foremost, for each value in each feature, we normalized the behavioral data of the seven features by

$$\tilde{x}_i = \frac{(x_i - \bar{x})}{\sqrt{\sigma}} \quad (1)$$

where x_i represents the i th data point for each of the seven behavioral features, $i = 1, 2, 3, \dots, n$. n is the number of points sampled from each feature in all groups. \bar{x} and $\sqrt{\sigma}$ represent the mean value and standard variance for each feature, respectively.

Second, we obtained the seven \tilde{x}_i values. Each group had positive and negative values, and the scale among these values was not fixed. Hence, we projected the features into an exponentiation expression, mapping these values in a unified scale (a unified vector space). For each feature depicted in a different group, we used equation (2) to process this step:

$$\tilde{x}_f = \frac{\text{average}(e^{\tilde{x}_i})}{\max(\text{average}(e^{\tilde{x}_i}))} \quad (2)$$

where $f = 1, 2, 3, \dots, 7$, represents the seven behavioral features in each group. We averaged the e^{x_i} in each group, obtaining lists with seven feature values in each group.

In the final analysis, we used the intact group values as the benchmark, significantly depicting the feature values' variance. We used equation (3) to process this step:

$$\tilde{x}_o = \frac{\tilde{x}_g}{\tilde{x}_{\text{intact}}} \quad (3)$$

where \tilde{x}_g represents each feature value in each group. $\tilde{x}_{\text{intact}}$ represents the feature values in the intact group, namely, the benchmark values.

Statistics

Multiple samples were analyzed by one-way or two-way analysis of variance (ANOVA). In this study, we used one-way ANOVA to compare data with only one factor (e.g., treatment) and two-way ANOVA to compare data with two factors (e.g., treatment and time). Differences between the two experimental group (e.g. control and MN-MS patch) were analyzed by Student's t test. All parameters were expressed as the mean \pm standard error of the mean (SEM), and a P value less than 0.05 was considered significant. Graphpad software (v8.3.0, USA) and Python package (SciPy, v1.4.1) were used for statistical analysis and visualization. Electromyography (EMG) data analysis and behavioral assessment were using MATLAB(v2020b). For microscopy, images were analyzed using Fiji (Windows 64, v1.51, NIH).

Reporting summary

Further information on research design is available in the Nature Portfolio Reporting Summary linked to this article.

Data availability

The data to support the findings of this study are included in the paper and supplementary information. The raw data for figures were provided in the supplementary source data file. Any additional requests for information can be directed to, and will be fulfilled by, the lead contact. Source data are provided with this paper.

Code availability

All figures were directly generated in MATLAB and Python from the code available at the GitHub repository at https://github.com/StarLight1212/NC_proj⁵⁸. The data used and generated in this study can be found at <https://drive.google.com/drive/folders/laz7uOLzP5xH7K-zpFzoAkv36kasVc-AW>.

References

- Collaborators G. N. Global, regional, and national burden of neurological disorders, 1990–2016: a systematic analysis for the Global Burden of Disease Study 2016. *Lancet Neurol.* **18**, 459–480 (2019).
- Liu, Z. et al. High-dose methylprednisolone for acute traumatic spinal cord injury: a meta-analysis. *Neurology* **93**, e841–e850 (2019).
- Inglis, T. et al. In-hospital mortality for the elderly with acute traumatic spinal cord injury. *J. Neurotrauma* **37**, 2332–2342 (2020).
- Ahuja, C. S. et al. Traumatic spinal cord injury. *Nat. Rev. Dis. Prim.* **3**, 1–21 (2017).
- Bains, M. & Hall, E. D. Antioxidant therapies in traumatic brain and spinal cord injury. *Biochim. Biophys. Acta* **1822**, 675–684 (2012).
- Anwar, M. A., Al Shehabi, T. S. & Eid, A. H. Inflammogenesis of secondary spinal cord injury. *Front. Cell Neurosci.* **10**, 24 (2016).
- Tahmasebinia, F. & Pourgholaminejad, A. The role of Th17 cells in auto-inflammatory neurological disorders. *Prog. Neuro-Psychopharmacol. Biol. Psychiatry* **79**, 408–416 (2017).
- Sahni, V. & Kessler, J. A. Stem cell therapies for spinal cord injury. *Nat. Rev. Neurol.* **6**, 363–372 (2010).
- Assinck, P., Duncan, G. J., Hilton, B. J., Plemel, J. R. & Tetzlaff, W. Cell transplantation therapy for spinal cord injury. *Nat. Neurosci.* **20**, 637–647 (2017).
- Shi, Y. et al. Immunoregulatory mechanisms of mesenchymal stem and stromal cells in inflammatory diseases. *Nat. Rev. Nephrol.* **14**, 493–507 (2018).
- Chhabra, H. S. & Sarda, K. Clinical translation of stem cell based interventions for spinal cord injury—are we there yet? *Adv. Drug Deliv. Rev.* **120**, 41–49 (2017).
- Fischer, U. M. et al. Pulmonary passage is a major obstacle for intravenous stem cell delivery: the pulmonary first-pass effect. *Stem Cells Dev.* **18**, 683–692 (2009).
- Schrepfer, S. et al. Stem cell transplantation: the lung barrier. *Transplant. Proc.* **39**, 573–576 (2007).
- Stenger, E. et al. Safety of autologous freshly expanded mesenchymal stromal cells for the treatment of graft-versus-host disease. *Front. Immunol.* **13**, 959658 (2022).
- Fischer, I., Dulin, J. N. & Lane, M. A. Transplanting neural progenitor cells to restore connectivity after spinal cord injury. *Nat. Rev. Neurosci.* **21**, 366–383 (2020).
- Riazifar, M. et al. Stem cell-derived exosomes as nanotherapeutics for autoimmune and neurodegenerative disorders. *ACS Nano* **13**, 6670–6688 (2019).
- Zhang, S. et al. MSC exosomes mediate cartilage repair by enhancing proliferation, attenuating apoptosis and modulating immune reactivity. *Biomaterials* **156**, 16–27 (2018).
- Phinney, D. G. & Pittenger, M. F. Concise review: MSC-derived exosomes for cell-free therapy. *Stem Cells* **35**, 851–858 (2017).
- Li, L. et al. Transplantation of human mesenchymal stem-cell-derived exosomes immobilized in an adhesive hydrogel for effective treatment of spinal cord injury. *Nano Lett.* **20**, 4298–4305 (2020).
- Li, L. et al. Stimulation by exosomes from hypoxia preconditioned human umbilical vein endothelial cells facilitates mesenchymal stem cells angiogenic function for spinal cord repair. *ACS Nano* **16**, 10811–10823 (2022).
- Mu, J. et al. Hypoxia-stimulated mesenchymal stem cell-derived exosomes loaded by adhesive hydrogel for effective angiogenic treatment of spinal cord injury. *Biomater. Sci.* **10**, 1803–1811 (2022).
- Cheng, L. & Hill, A. F. Therapeutically harnessing extracellular vesicles. *Nat. Rev. Drug Discov.* **21**, 379–399 (2022).
- Mukherjee, N., Adak, A. & Ghosh, S. Recent trends in the development of peptide and protein-based hydrogel therapeutics for the healing of CNS injury. *Soft Matter* **16**, 10046–10064 (2020).
- Huang, J. et al. 3D-printed polypyrrole microneedle arrays for electronically controlled transdural drug release. *ACS Biomater. Sci. Eng.* **8**, 1544–1553 (2022).
- Wang, Z. et al. Silk microneedle patch capable of on-demand multidrug delivery to the brain for glioblastoma treatment. *Adv. Mater.* **34**, e2106606 (2022).
- Li, W. et al. Rapidly separable microneedle patch for the sustained release of a contraceptive. *Nat. Biomed. Eng.* **3**, 220–229 (2019).
- Xue, F. et al. Electroconductive and porous graphene-xanthan gum gel scaffold for spinal cord regeneration. *Eur. Polym. J.* **173**, 111225 (2022).
- Seidlits, S. K. et al. The effects of hyaluronic acid hydrogels with tunable mechanical properties on neural progenitor cell differentiation. *Biomaterials* **31**, 3930–3940 (2010).
- Ying, G. et al. Bioprinted injectable hierarchically porous gelatin methacryloyl hydrogel constructs with shape-memory properties. *Adv. Funct. Mater.* **30**, 2003740 (2020).
- Zhu, J. et al. Gelatin methacryloyl microneedle patches for minimally invasive extraction of skin interstitial fluid. *Small* **16**, e1905910 (2020).

31. Wechsler, M. E., Rao, V. V., Borelli, A. N. & Anseth, K. S. Engineering the MSC secretome: a hydrogel focused approach. *Adv. Healthc. Mater.* **10**, e2001948 (2021).
32. Lai, J. J. et al. Exosome processing and characterization approaches for research and technology development. *Adv. Sci.* **9**, e2103222 (2022).
33. Ye, J. et al. Rationally designed, self-assembling, multifunctional hydrogel depot repairs severe spinal cord injury. *Adv. Healthc. Mater.* **10**, e2100242 (2021).
34. Basso, D. M., Beattie, M. S. & Bresnahan, J. C. Graded histological and locomotor outcomes after spinal cord contusion using the NYU weight-drop device versus transection. *Exp. Neurol.* **139**, 244–256 (1996).
35. Brommer, B. et al. Improving hindlimb locomotor function by Non-invasive AAV-mediated manipulations of propriospinal neurons in mice with complete spinal cord injury. *Nat. Commun.* **12**, 781 (2021).
36. Chuiko, G. P., Dvornik, O. V. & Darnapak, Y. S. Shape evolutions of poincare plots for electromyograms in data acquisition dynamics. In: *2nd IEEE International Conference on Data Stream Mining and Processing (DSMP)* (IEEE, 2018).
37. Fu, Y. et al. Emerging understanding of apoptosis in mediating mesenchymal stem cell therapy. *Cell Death Dis.* **12**, 596 (2021).
38. Dazzi, F. & Galleu, A. Apoptosis in mesenchymal stromal cells induces in vivo recipient-mediated immunomodulation. *Sci. Transl. Med.* **9**, eaam7828 (2017).
39. Preda, M. B. et al. Short lifespan of syngeneic transplanted MSC is a consequence of in vivo apoptosis and immune cell recruitment in mice. *Cell Death Dis.* **12**, 566 (2021).
40. Huang, J.-H. et al. Systemic administration of exosomes released from mesenchymal stromal cells attenuates apoptosis, inflammation, and promotes angiogenesis after spinal cord injury in rats. *J. Neurotrauma* **34**, 3388–3396 (2017).
41. Cao, Y. et al. Local delivery of USC-derived exosomes harboring ANGPTL3 enhances spinal cord functional recovery after injury by promoting angiogenesis. *Stem Cell Res. Ther.* **12**, 1–17 (2021).
42. Yan, C. et al. Human umbilical cord mesenchymal stem cell-derived exosomes accelerate diabetic wound healing via ameliorating oxidative stress and promoting angiogenesis. *Front. Bioeng. Biotechnol.* **10**, 829868 (2022).
43. Ruan, J., Miao, X., Schluter, D., Lin, L. & Wang, X. Extracellular vesicles in neuroinflammation: Pathogenesis, diagnosis, and therapy. *Mol. Ther.: J. Am. Soc. Gene Ther.* **29**, 1946–1957 (2021).
44. Wang, B. et al. Mesenchymal stem cells deliver exogenous MicroRNA-let7c via exosomes to attenuate renal fibrosis. *Mol. Ther. J. Am. Soc. Gene Ther.* **24**, 1290–1301 (2016).
45. Pinho, A. G. et al. Immunomodulatory and regenerative effects of the full and fractioned adipose tissue derived stem cells secretome in spinal cord injury. *Exp. Neurol.* **351**, 113989 (2022).
46. Wang, X. et al. Comparison of extruded cell nanovesicles and exosomes in their molecular cargos and regenerative potentials. *Nano Res.* **16**, 7248–7259 (2023).
47. Jeppesen, D. K. et al. Reassessment of exosome composition. *Cell* **177**, 428–445.e418 (2019).
48. Kirillova, A. et al. Fabrication of biomedical scaffolds using biodegradable polymers. *Chem. Rev.* **121**, 11238–11304 (2021).
49. Xing, J. F., Zheng, M. L. & Duan, X. M. Two-photon polymerization microfabrication of hydrogels: an advanced 3D printing technology for tissue engineering and drug delivery. *Chem. Soc. Rev.* **44**, 5031–5039 (2015).
50. Jiang, X. et al. Embryonic stem cell-derived mesenchymal stem cells alleviate skeletal muscle injury induced by acute compartment syndrome. *Stem Cell Res. Ther.* **13**, 313 (2022).
51. Au Yeung, C. L. et al. Exosomal transfer of stroma-derived miR21 confers paclitaxel resistance in ovarian cancer cells through targeting APAF1. *Nat. Commun.* **7**, 11150 (2016).
52. Kenney, R. M., Loeser, A., Whitman, N. A. & Lockett, M. R. Paper-based transwell assays: an inexpensive alternative to study cellular invasion. *Analyst* **144**, 206–211 (2018).
53. Zhao, K. Effect of pore size and porosity on the cytocompatibility of porous titanium. *Clin. Oral. Implants Res.* **31**, 76–76 (2020).
54. Bala, E. et al. Motor and somatosensory evoked potentials are well maintained in patients given dexmedetomidine during spine surgery. *Anesthesiology* **109**, 417–425 (2008).
55. Iyer, S., Maybhathe, A., Presacco, A. & All, A. H. Multi-limb acquisition of motor evoked potentials and its application in spinal cord injury. *J. Neurosci. Methods* **193**, 210–216 (2010).
56. Waterstraat, G., Körber, R., Storm, J. H. & Curio, G. Noninvasive neuromagnetic single-trial analysis of human neocortical population spikes. In: *Proc. Natl Acad. Sci. USA* **118** (2021).
57. Liu, S. et al. Fully passive flexible wireless neural recorder for the acquisition of neuropotentials from a rat model. *ACS Sens.* **4**, 3175–3185 (2019).
58. Fang, A. et al. Porous microneedle patch with sustained delivery of extracellular vesicles mitigates severe spinal cord injury. *bioRxiv* <https://doi.org/10.1101/2022.07.18.500400> (2023).

Acknowledgements

This study was supported by the Scientific and Technological Innovation 2030 Program of China—major projects (2021ZD0200408 to X.W.), the National Natural Science Foundation of China (81971866 to X.W.), the Science Fund for Distinguished Young Scholars of Zhejiang Province (LR20H090002 to X.W.), the Leading Innovative and Entrepreneur Team Introduction Program of Zhejiang (2019R01007 to X.W.), the Fundamental Research Funds for the Central Universities (K20210195 to X.W.) and the Postdoctoral General Foundation project (2020M671746 to X.C.).

Author contributions

A.F., Y.-F.W., N.G., and Y. Z., contributed equally to this work. X.W. and A.F. conceptualized and designed the study. A.F., Y.-F.W., N.G. conducted the experiments and collected the data. A.F., Y.-F.W., N.G., Y. Z., L. L., B. G., A.M., Y.W., X.L., W.C., X.C., J. Y., Z.A., X.-D.L., H.Z., Z.W., S.J., K.X., Y.H., X.G., B.Y., and X.W. analyzed and interpreted the data. A.F., Y. Z., and X.W. drafted the paper. All authors critically revised the manuscript and approved the final version for submission.

Competing interests

Zhejiang University has filed a patent application (application number: 2022108442387, applied) related to this work, with X.W., A.F., and B.G. listed as inventors. X.W. is a scientific co-founder of WeQure AI Ltd. All the other authors declare no competing interests.

Additional information

Supplementary information The online version contains supplementary material available at <https://doi.org/10.1038/s41467-023-39745-2>.

Correspondence and requests for materials should be addressed to Xuhua Wang.

Peer review information *Nature Communications* thanks Sebastien Couillard-despres, Karen Lankford and the other, anonymous, reviewer(s) for their contribution to the peer review of this work.

Reprints and permissions information is available at <http://www.nature.com/reprints>

Publisher's note Springer Nature remains neutral with regard to jurisdictional claims in published maps and institutional affiliations.

Open Access This article is licensed under a Creative Commons Attribution 4.0 International License, which permits use, sharing, adaptation, distribution and reproduction in any medium or format, as long as you give appropriate credit to the original author(s) and the source, provide a link to the Creative Commons license, and indicate if changes were made. The images or other third party material in this article are included in the article's Creative Commons license, unless indicated otherwise in a credit line to the material. If material is not included in the article's Creative Commons license and your intended use is not permitted by statutory regulation or exceeds the permitted use, you will need to obtain permission directly from the copyright holder. To view a copy of this license, visit <http://creativecommons.org/licenses/by/4.0/>.

© The Author(s) 2023, corrected publication 2023